



# Nanoparticles Application in Promoting the Growth of a More Protective Oxide Scale at High Temperatures

Xiao Peng<sup>1,2</sup> · Yuanchao Huang<sup>3,4</sup> · Xiaolan Wang<sup>5</sup> · Yun Xie<sup>1,2</sup>

Received: 28 July 2023 / Revised: 24 August 2023 / Accepted: 26 August 2023 /  
Published online: 12 September 2023

© The Author(s), under exclusive licence to Springer Science+Business Media, LLC, part of Springer Nature 2023

## Abstract

Owing to a very high surface-to-volume ratio, nanoparticles (NPs) have unique physical and chemical properties distinguishable from those of their bulk counterparts. They have become innovative constituents in the strategy of designing and developing advanced functional materials and medical materials. So far, there have been few studies on the theory and practice of applying NPs to promote the growth of a more protective oxide scale at high temperatures. In this contribution, we report the research progress by application of specific metal and metal oxide NPs in: (i) developing chromia- and alumina-forming coatings; (ii) facilitating the selective oxidation of alloys; (iii) assisting direct thermal growth of  $\alpha$ -alumina on Ni–Al intermetallic compounds; and (iv) increasing the oxidation resistance of thermally-grown oxides.

**Keywords** High temperature oxidation · Coating · Nanoparticle

---

✉ Xiao Peng  
xpeng@nchu.edu.cn

<sup>1</sup> School of Materials Science and Engineering, Nanchang Hangkong University, 696 Fenghenan Avenue, Nanchang 330063, China

<sup>2</sup> Jiangxi Provincial Engineering Research Center for Surface Technology of Aeronautical Materials, Nanchang Hangkong University, 696 Fenghenan Avenue, Nanchang 330063, China

<sup>3</sup> State Key Laboratory of Silicon Materials, School of Materials Science and Engineering, Zhejiang University, Hangzhou 310027, Zhejiang, China

<sup>4</sup> Institute of Advanced Semiconductors, Hangzhou Innovation Center, Zhejiang University, Hangzhou 311200, Zhejiang, China

<sup>5</sup> Laboratory for Corrosion and Protection, Institute of Metal Research, Chinese Academy of Sciences, Shenyang 110016, China

## Introduction

Many nanostructured/nanocrystalline (NC) materials have unique and generally improved physical, chemical, and mechanical properties in comparison to their polycrystalline counterparts. This is largely due to the former being composed of crystallites in nanometer scale (typically < 100 nm) and consequently a large fractions of atoms (up to 50%) at grain boundaries (GBs). In the past three to four decades, researchers have paid great attention to the application and development of NC materials with enhanced hardness, abrasion wear resistance, strength-toughness balance and corrosion performance [1–5]. For example, many NC alloys have the advantage over normally micro-grained counterparts in the ability of thermally growing a protective scale of oxide such as  $\text{Cr}_2\text{O}_3$  and  $\text{Al}_2\text{O}_3$ , because abundant GBs in the alloys accelerate the diffusion of Cr and Al to oxidation front [6]. The latter is beneficial to minimize the critical concentration of Cr ( $N_{\text{Cr}}^*$ ) and Al ( $N_{\text{Al}}^*$ ) for the selective oxidation of the corresponding element, on a basis of Wagner's classic oxidation theory expressed by the equation below for a single-phase binary alloy [7]:

$$N_m^* = \left( \frac{\pi g^* N_O^S N_O D_O V_m}{2\eta D_m V_{\text{ox}}} \right)^{1/2} \quad (1)$$

where  $g^*$  is a constant,  $N_O^S$ ,  $N_O$  is the concentration of oxygen at the surface and in the alloy,  $\eta$  is a constant which is equal to  $y/x$  for the formed  $\text{M}_x\text{O}_y$ ,  $D_O$  and  $D_m$  are the diffusivities of oxygen and more active metal (Cr or Al here) in the alloy, and  $V_m$  and  $V_{\text{ox}}$  are molar volume of the alloy and oxide of the more active metal ( $\text{Cr}_2\text{O}_3$  or  $\text{Al}_2\text{O}_3$ ), respectively. Nanocrystallization of a coarse-grained alloy would convert it from an oxidation-nonresistant alloy to a  $\text{Cr}_2\text{O}_3$  and  $\text{Al}_2\text{O}_3$  former. For improving high temperature corrosion resistances, techniques to either nanocrystallize the alloy surface (e.g., surface mechanical attrition [8], shot peening [9, 10], particle impact [8, 11], etc.) or deposit a NC coating onto the alloy (e.g., physical vapour deposition and sputtering [12–16], chemical vapour deposition [17, 18], plasma spraying [19–21], high velocity oxygen fuel [21, 22] and electrochemical deposition [22–26]) have been so far extensively explored by the research community.

Nanoparticles are another important category of nanostructured materials. They are actually build-up from full-shell atoms cluster with cubic or hexagonal close-packed (hcp) structure, normally evolving from atoms and ions in either a vapor or a liquid state through fundamental steps of nucleation, coalescence and growth [4]. Owing to a very high surface-to-volume ratio, i.e., large fractions of atoms locating at surface, NPs have unique physical, chemical and biological properties distinguishable from those of their bulk counterparts. They constitute one of the most fundamental and creative elements of the strategies for designing and developing advanced nanomaterials in the progress of science and technology.

Metallic NPs, most of which are noble metals such as Ag, Au, Pt, Pd, and Cu, have been by and large intergraded into organic and inorganic substrates to form novel functional nanocomposites exploited in optical [27–29], electrical [29–32], magnetic [33, 34], catalytic [35, 36], and energy storage [37, 38] applications and

for antibacterial [28, 39] purposes. Differently, NPs of active metals like Zn [40, 41], Ti [42, 43] and Al [44, 45], have normally been dispersed into epoxy resins to form novel corrosion-resistant polymer-based nanocomposites coatings in liquid mediums, in which the metallic NPs with lower corrosion potentials offer cathodic protection and those dispersion causing densification of the polymers offer better barrier protection to the corrosion species permeation. Al NPs are also used as effective combustible additives in propellant formulations for dramatically higher and faster energy release [46]. They may have profound opportunity in the high-capacity hydrogen storage materials development.

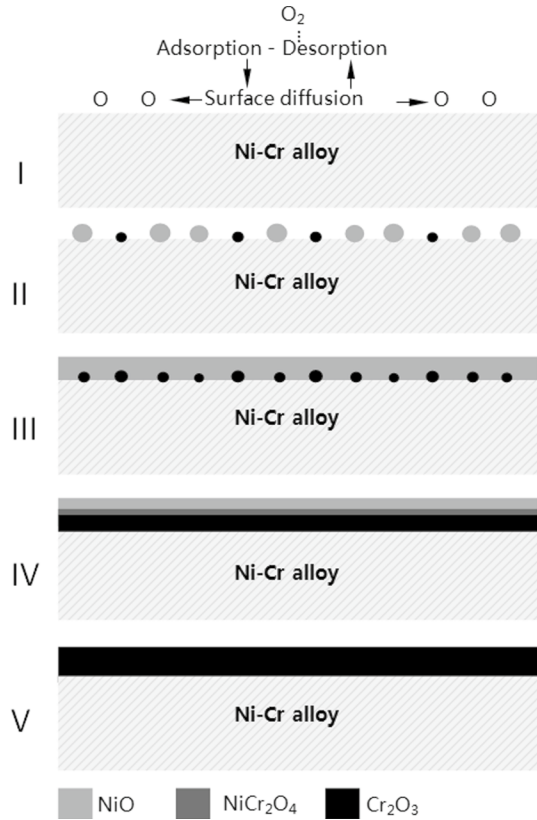
Compared to metal NPs, metal oxide NPs exhibit unique antioxidant and catalytic properties, high chemical stability, and good biocompatibility, etc. They have received great attentions for applications in the fields of biology, catalysts, biomedical engineering, energy conversion, semiconductor, magnetism, and optics, etc. For instances, TiO<sub>2</sub> NPs are used as novel antimicrobial agents [47] and also applied to photocatalysis, solar cells, drug delivery [48]. Cr<sub>2</sub>O<sub>3</sub> NPs can be used in many fields, such as pigment, catalyst, lithium material etc. [49]. Oxide NPs of Ce, which is one of the most reactive and copious rare elements, have been explored for diverse applications in catalysis, fuel cells, gas sensors, ultraviolet (UV) absorbers, energy storage devices, optical devices, sensing, medicine, imaging, antioxidants, free radical scavengers, etc. [50].

Despite metal and metal oxide NPs having been widely applied to the functional materials and medical materials, they are rarely added to metallic structure materials and coatings for improving their resistance to high temperature corrosion. In this contribution, we report some progresses made in the field of NPs application in developing chromia- and alumina-forming coatings (Section “[Application in Developing Chromia- and Alumina-forming Coatings](#)”), catalyzing the selective oxidation of alloys (Section “[Catalyzing the Selective Oxidation of Alloys](#)”), assisting direct thermal growth of  $\alpha$ -alumina on Ni–Al intermetallic compounds (Section “[Assisting Direct Thermal Growth of  \$\alpha\$ -Alumina on Ni–Al Intermetallics](#)”), and increasing the oxidation resistance of thermally-grown oxides (TGOs) (Section “[Increasing the Oxidation Resistance of Thermally-grown Oxides](#)”).

## Application in Developing Chromia-and Alumina-Forming Coatings

Based on our knowledge to selective oxidation of alloys [51], the oxidation progression for the formation of chromia can, if taking a Ni–Cr binary alloy as an example, be divided into several steps: (i) Adsorption to the metal surface of oxygen gas and its dissociation and diffusion on the surface, (ii) Formation of NiO and Cr<sub>2</sub>O<sub>3</sub> nuclei, (iii) Development of a top thin layer of NiO due to rapid lateral growth of NiO nuclei, (iv) Lateral growth of Cr<sub>2</sub>O<sub>3</sub> nuclei to develop a continuous layer, and (v) Steady-state growth of this oxide layer normal to the metal surface. The Cr selective oxidation process is schematically shown in Fig. 1. Among the five steps, step *iv* appears to be pivotal to the conversion of the Ni–Cr alloy from a NiO former to a Cr<sub>2</sub>O<sub>3</sub> former. If Cr<sub>2</sub>O<sub>3</sub> can copiously nucleate from the onset of oxidation, the oxygen partial pressure ( $p_{O_2}$ ) at the oxidation front of the alloy sharply decreases.

**Fig. 1** A schematic drawing of Cr selective oxidation process of a Ni–Cr binary alloy



This thermodynamically suppresses the growth of NiO and the latter is consequently undermined by Cr<sub>2</sub>O<sub>3</sub> [51, 52].

From the above consideration, we wondered that a chromia scale would easier develop on a Ni–Cr coating if it has a microstructure with the merits of ubiquitously nucleating Cr<sub>2</sub>O<sub>3</sub> from the onset of oxidation. Figure 2a schematically demonstrates such a typical microstructure of the Ni–Cr coating, in which the Cr particles with an averaged interparticle spacing ( $\xi$ ) are distributed over the Ni matrix. Assuming that the particles are spherical with a radius of  $r$  and their spatial distribution in a unit cell follows a simple cubic structure,  $\xi$  is a function of  $r$  which is expressed by [53]

$$\xi = \left[ \sqrt[3]{\frac{4\pi}{3V}} - 2 \right] r \quad (2)$$

where  $V$  is the volume fraction of Cr particles. The dependence of  $\xi$  on  $r$  following Eq. (2) is shown in Fig. 2b. At a given  $V$ ,  $\xi$  can be easily reduced from micro-length scale to nano-length scale if a metal is dispersed with Cr NPs rather than microparticles (MPs). For example,  $\xi$  decreases from 3  $\mu\text{m}$  to only 30 nm with decreasing

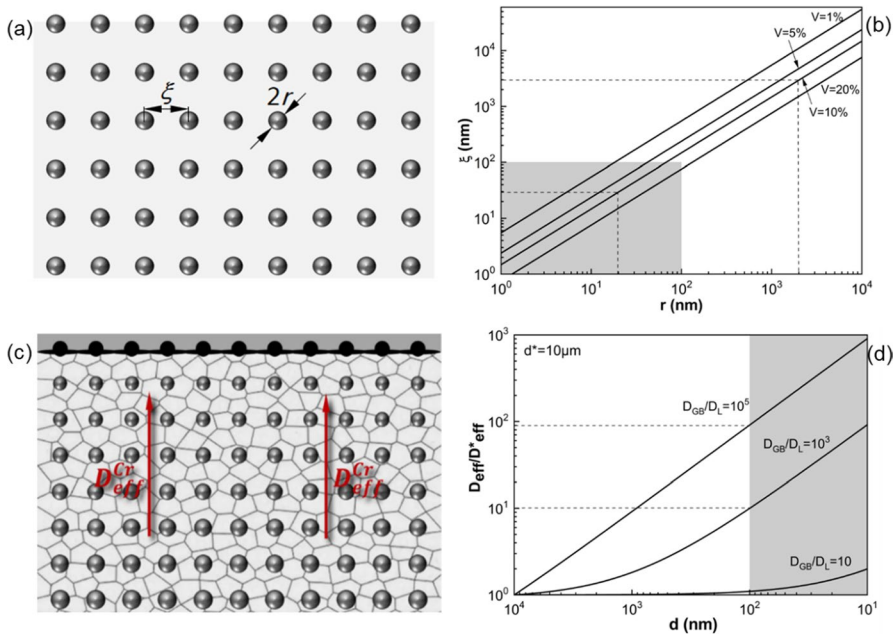


**Fig. 2** **a** A schematic drawing of a Ni–Cr coating dispersing Cr particles with radius of  $\gamma$  and interparticle spacing of  $\xi$ , **b** dependence of  $\xi$  on  $\gamma$  assuming the particle spatial distribution following a simple cubic structure, **c** a schematic showing development of a continuous chromia scale on the coating is intrinsically associated with  $\xi$  and effective diffusivity  $D_{\text{eff}}$  of Cr, and **d** variation of  $D_{\text{eff}}$  with a decrease of the coating’s grain size of  $d$  ( $D_{\text{eff}}^*$  in the alloy with a grain size of 10  $\mu\text{m}$  for comparison)

particle size from 2  $\mu\text{m}$  to 20 nm at  $V=10\%$  (see the dashed line in Fig. 2). Increasing  $V$  can further decrease the value of  $\xi$  at a given  $r$ . Therefore, dispersing Cr NPs into the two-phase Ni–Cr coating should theoretically increase the capability of thermally growing  $\text{Cr}_2\text{O}_3$ . When oxidation starts, the Cr NPs at and close to the surface act as the sites for “diffusionlessly” nucleating  $\text{Cr}_2\text{O}_3$ . As presented in a Fig. 2c, the smaller the value of  $\xi$  at a given  $V$ , the more copious the  $\text{Cr}_2\text{O}_3$  nuclei, the easier the step *iv* to be achieved. Moreover, chromia lateral growth can be promoted in a fine-grained Ni matrix, because the increased GBs accelerate Cr diffusion toward the oxidation front (Fig. 1c). The effective diffusivity ( $D_{\text{eff}}$ ) of Cr in the fine-grained Ni can be expressed by a summation of lattice ( $D_l$ ) and GB diffusivity ( $D_{\text{gb}}$ ) as given below

$$D_{\text{eff}} = (1 - f)D_l + fD_{\text{gb}} \tag{3}$$

where  $f$  is the GB area fraction and equals  $2\delta/d$  ( $\delta$  is the GB width and  $d$  the grain size of the metal matrix). If assuming the metal grains as cubic, Eq. (3) is simplified as

$$D_{\text{eff}} = D_l + \frac{2\delta}{d}D_{\text{gb}} \tag{4}$$

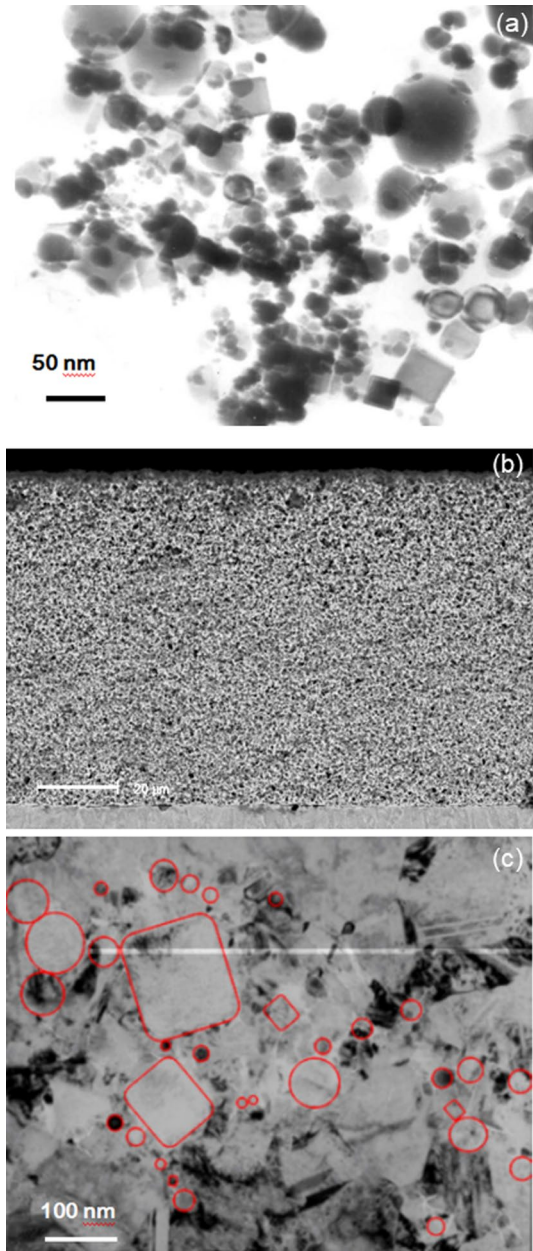
The  $D_{\text{eff}}$  increase with decreasing the metal matrix grain size is illustrated in Fig. 2d, where  $D_{\text{eff}}^*$  is regarded as the effective diffusivity of Cr in the Ni–Cr alloy with a grain size of 10  $\mu\text{m}$  for comparison. Clearly, the  $D_{\text{eff}}/D_{\text{eff}}^*$  ratio is dramatically increased when the grain size is decreased down to the nano-regime. For example, if  $d$  is reduced from the reference 10  $\mu\text{m}$  to 100 nm,  $D_{\text{eff}}$  becomes 1 order of magnitude larger than  $D_{\text{eff}}^*$  in the case of  $D_l/D_{\text{gb}} = 10^3$ .

Electrodeposition is a method to introduce a second-phase particle into a metal matrix [54]. It can also make the metal matrix nanocrystallized [55]. Accordingly through loading an appropriate amount of the NPs into a conventional Ni-plating electrolytic bath, a NC Ni matrix coating dispersing Cr NPs were compositely electroplated [24, 56]. It is noteworthy that a perforated plate moves up and down to prevent not only sedimentation but also agglomeration of the NPs in bath during electrodeposition [23]. Figure 3a shows the transmission electron microscopy (TEM) image of the as-received Cr NPs, most of which were spherical but some appeared to be cubic. Here, it is noteworthy that the metal NPs normally have an oxide film with a thickness in a few nanometers range [24]. The microstructure of the Ni–Cr coating dispersing the Cr NPs is presented in Fig. 3b. The Cr NPs with a mean  $\xi$  in a nanolength scale were randomly distributed over a NC Ni matrix. The electrodeposited coating was compact, without pores or cracks observed at the particles/Ni interface. Figure 3c displays the cross-sectional morphology of an electrodeposited Ni–Cr coating with Cr NPs of 13.0 vol.% (10.8 wt.%). The coating was etched and the dark pitting dots corresponded to the areas rich in Cr NPs [53]. Obviously, Cr NPs were homogeneously distributed over the Ni matrix.

Shown in Fig. 4a is the oxidation kinetics of a Ni–Cr coating (mean Cr particle size:  $\sim 25$  nm) at 900  $^\circ\text{C}$  in air for 20 h. Oxidation curve of a Ni–20Cr alloy which is well-known as a  $\text{Cr}_2\text{O}_3$  former is presented for comparison. The coating dispersing 6.6 wt.%Cr NPs was oxidized faster than a pure Ni coating, which was electrodeposited from the same bath but without loading NPs and thermally grew a porous NiO scale (Fig. 4b). There are several reasons for this. First, Cr NPs were easily oxidized into  $\text{Cr}_2\text{O}_3$  NPs which were then dispersed in the formed NiO scale. Second, the dispersion of  $\text{Cr}_2\text{O}_3$  NPs would cause grain refinement of the NiO scale, which accelerated the diffusion of Ni cations and O anions through the increased GBs in the oxide scale. Third, NiO is a well-known metal-deficient p-type semiconductor and its thermal growth is dominated by the diffusion of the principal Ni cation vacancies and, the latter concentration is increased with the incorporation of high valence Al cations [51]. When the Cr NPs content was increased to 7.8 wt.%, the Ni–Cr coating had a weight gain even slightly lower than the Ni-20Cr alloy, suggesting that the former had the ability of developing a  $\text{Cr}_2\text{O}_3$  scale. The oxidation rate of the coating was further reduced when the Cr NPs content was increased from 7.8 to 8.7 wt.%, because the latter Cr concentration led to the formation of purer  $\text{Cr}_2\text{O}_3$  scale (Fig. 4c) [57].

Based on previous works [24, 56–58], the particle-size-dependent critical Cr content ( $N_{\text{Cr}}^*$ ) of the Ni–Cr coating locates in the shadowed area presented in Fig. 5.  $N_{\text{Cr}}^*$  for the Cr NP-dispersed coating to form a  $\text{Cr}_2\text{O}_3$  scale is around and below 10

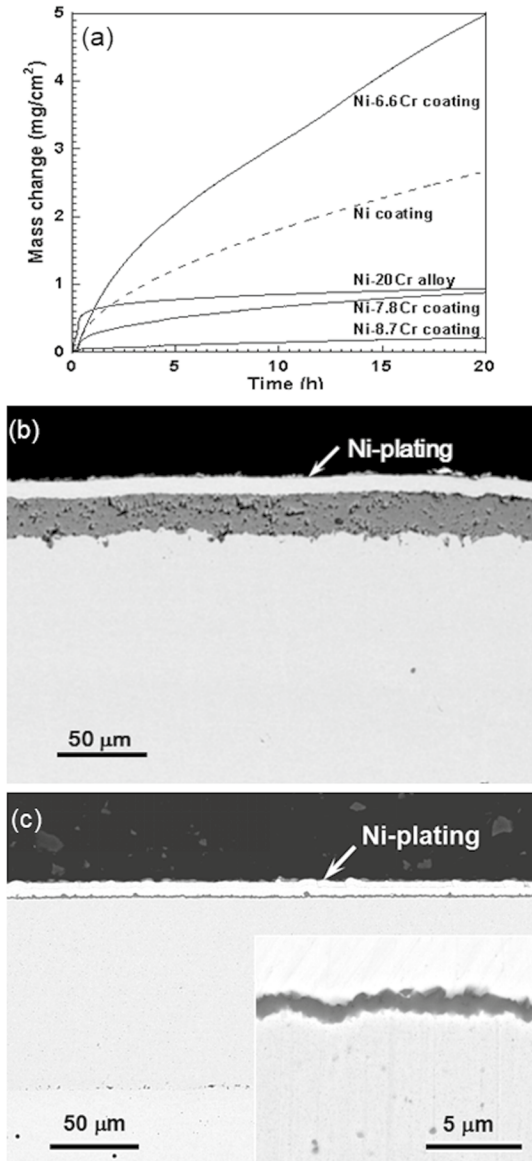
**Fig. 3** TEM BF image of **a** Cr NPs and **b** the Ni–Cr coating dispersing Cr NPs, **c** SEM cross-sectional morphology of the Ni–Cr coating (etched) [54]



wt.%, much lower than 20 wt.% needed by the Ni–Cr binary alloy. If Cr MPs are used to prepare the coating, the value of  $N_{Cr}^*$  is higher than 20 wt.%. Thus, compared to the conventional Ni–Cr alloy, the Ni–Cr coating dispersing MPs has a decreased while the one dispersing Cr NPs has an increased capability to grow a  $Cr_2O_3$  scale. The result coincides well with our aforementioned concept (Fig. 1) for structural



**Fig. 4 a** Oxidation kinetics of Cr NPs-dispersed Ni–Cr coating and arc-melted Ni–20Cr alloy in air at 900 °C and **b, c** SEM cross-sectional morphologies of the Ni coating **b** without and **c** with 8.7 wt.% Cr nanodispersions after 20 h oxidation in air at 900 °C [57]. The inset in (c) is a magnified view of the chromia scale



designing the chromia-forming coating by application of Cr NPs. More experimental evidences are summarily presented below.

The Ni-27Cr coating containing ~4 μm-sized Cr particles is a Cr<sub>2</sub>O<sub>3</sub> former [57]. The oxide formed after 20 h in air at 900 °C exhibits various oxide crystals on the surface (Fig. 6a). The finest oxide crystals are Cr<sub>2</sub>O<sub>3</sub> formed on the surface Cr MPs. The other larger crystals are NiO and NiCr<sub>2</sub>O<sub>4</sub> spinel formed between the Cr particles. The oxide scale is uneven in thickness (Fig. 6b). This is different from the



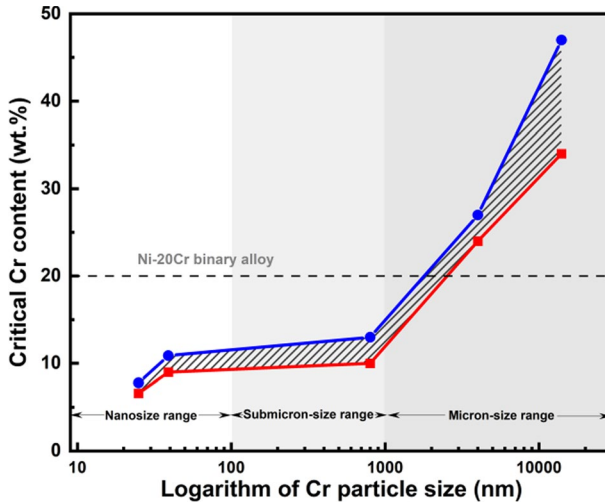
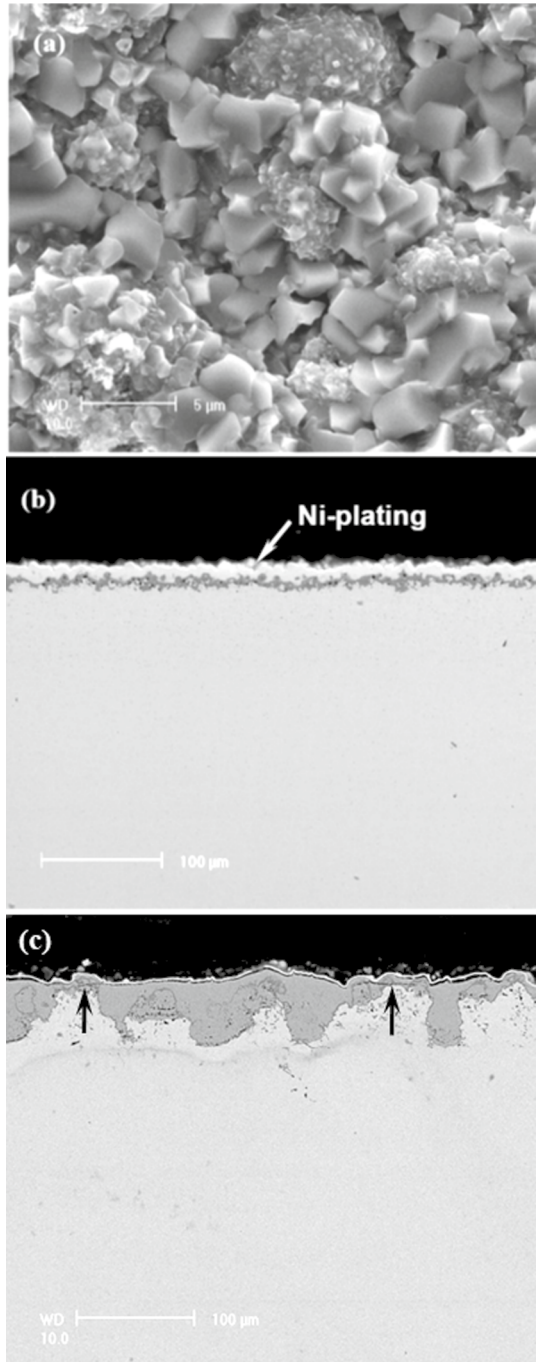


**Fig. 5** Dependence of the Cr particle size on the Cr content (in weight percentage) for Cr particles-dispersed Ni-Cr coating to thermally grow a chromia scale

Ni-8.7Cr coating dispersing Cr NPs, which grew a more flat  $\text{Cr}_2\text{O}_3$  scale with a uniform thickness (Fig. 4c). The latter is attributed to a rapid establishment of a continuous  $\text{Cr}_2\text{O}_3$  layer on the coating prepared by application of Cr NPs instead of Cr MPs, which decreases roughening kinetics of the coating during oxidation [59]. The Ni-24Cr coating grew an oxide scale with the thickness varied significantly from place to place (Fig. 6c), because it is difficult to form a  $\text{Cr}_2\text{O}_3$  layer during the initial and transient stage of oxidation. Thin discontinuous  $\text{Cr}_2\text{O}_3$  layers were actually seen in the thicker NiO scale, as some indicated by arrows.

Therefore, the unique ability of growing a  $\text{Cr}_2\text{O}_3$  layer from the onset of oxidation is the fundamental reason that the Cr NP-dispersed coating with a Cr content below 10 wt.% is still oxidation-resistant. Figure 7 shows the TEM observation of a Ni-10.9Cr coating (Cr particle size: ~39 nm), which was oxidized in air at 900 °C for only 30 min and cross-sectioned after Pt plating using a technique of focused ion beam (FIB). The coating has formed a  $\text{Cr}_2\text{O}_3$  scale, on a basis of X-ray mappings of the concerned elements (Fig. 7a). The initially-formed  $\text{Cr}_2\text{O}_3$  scale is not uniform in thickness. Thicker chromia is assumed to be the result of oxidation of the NP agglomerates at and close to the surface. It is plausible that part Cr NPs remained agglomerated during their retention period and the coating process. Viewed under higher magnifications (Fig. 7b), the  $\text{Cr}_2\text{O}_3$  scale was covered with  $\text{NiCr}_2\text{O}_4$  on some locations. It implies that the initially formed NiO formed between Cr NPs was quickly undermined by the underlying chromia. Afterwards, the NiO stopped growing and then transformed into the spinel oxide by diffusion reaction with chromia. The rapid formation is responsible for better hot corrosion resistance of the nanocomposite type Ni-11Cr coating than Ni-20Cr alloy under molten salts of  $\text{Na}_2\text{SO}_4\text{-K}_2\text{SO}_4\text{-NaCl}$  [60].

**Fig. 6** **a** SEM surface and **b, c** cross-sectional morphologies of the oxide scales on **(a, b)** Cr MPs-dispersed Ni-27Cr and **c** Ni-24Cr coatings for 20 h in air at 900 °C [57]



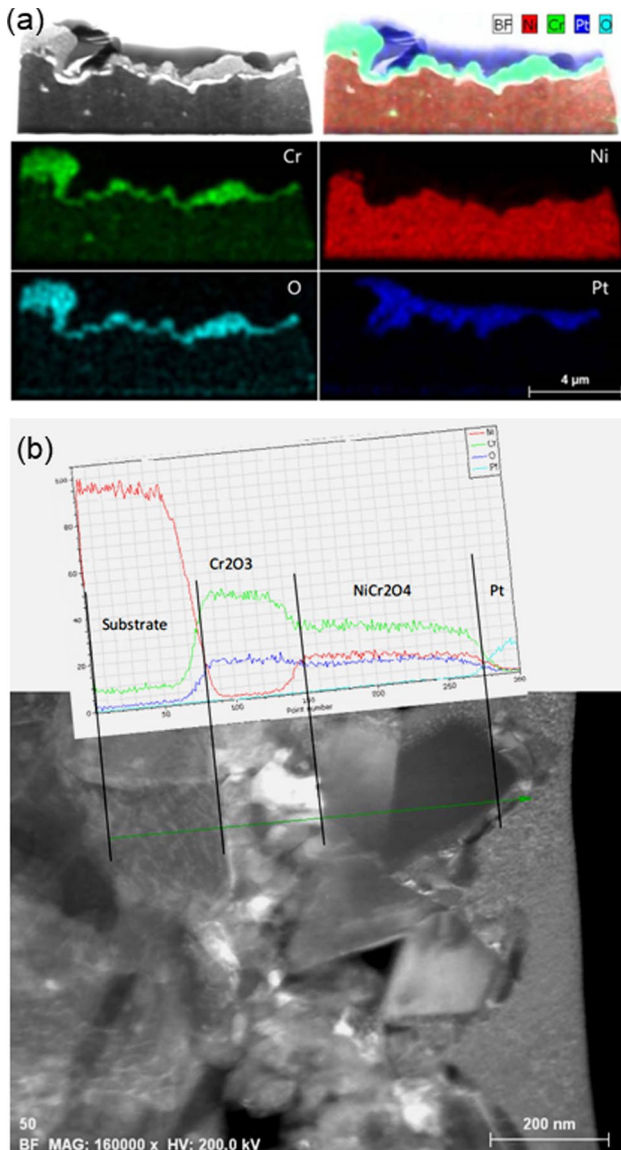


**Fig. 7** **a** Backscattered electron image (BEI) and corresponding elemental mappings of a Cr NPs-dispersed Ni-10.9Cr cross-sectioned by FIB after 30 min in air at 900 °C, showing the formation of a chromia scale. **b** TEM image and elemental distribution along the green line crossing the scale, indicative of the formation of the spinel oxide above chromia

Cu-based Cu-Ni-Cr alloys are generally not oxidation resistant, because the negligible solubility of Cr in the Cu matrix heavily restricts diffusion of Cr in the alloys [61, 62]. For example, a mechanically alloyed (MA) Cu-20Ni-20Cr alloy, although it had an average grain size of 80 nm after hot pressing and annealing,

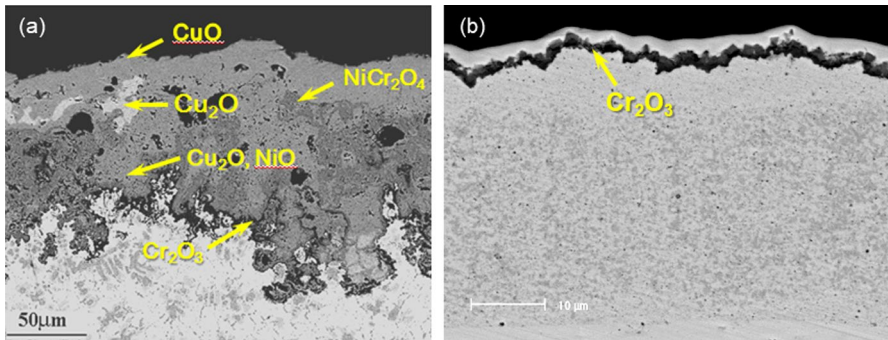


**Fig. 8** Cross-sectional morphologies of the oxide scales on **a** mechanically alloyed Cu-20Ni-20Cr alloy for 24 h oxidation [63] and **b** electrodeposited Cu-30Ni-20Cr coating for 20 h at 800 °C [65]

formed a thicker oxide mixture scale consisting of CuO, Cu<sub>2</sub>O, NiO, NiCr<sub>2</sub>O<sub>4</sub> and Cr<sub>2</sub>O<sub>3</sub> during oxidation in air at 800 °C (Fig. 8a) [63]. Although the diffusivity of Cr is increased with increasing the Ni concentration, the MA Cu-40Ni-20Cr alloy (with an average grain size of 30 nm) appeared not to grow a Cr<sub>2</sub>O<sub>3</sub> layer until a thicker double-layered scale of CuO and NiCr<sub>2</sub>O<sub>4</sub> had formed. However, under the same oxidation temperature, a Cr<sub>2</sub>O<sub>3</sub> scale occurred on the Cu-40Ni-20Cr [64] and Cu-30Ni-20Cr coatings [65] with a mean grain size of 60 nm prepared by composite electrodeposition of Cu-Ni alloy with Cr NPs, as one typical feature presented in Fig. 8b. The comparison result demonstrates that the nanoscale dispersion of Cr NPs may be a more important factor than the coating nanocrystallization in promoting the formation of a Cr<sub>2</sub>O<sub>3</sub> scale. It has also been found that the electrodeposited NC Cu-30Ni-20Cr coating with the nanoscale Cr distribution displayed an oxidation rate lower than sputter-deposited and mechanical-attrition-treated compositional-similar nanocrystalline coatings with atomic- and micron-scale dispersion uniformity of Cr, respectively [8]. It appears that the nanoscale  $\xi$  (see Eq. 2) is the key reason for the enhanced capability of the Cr NPs-dispersed ternary coatings to grow a Cr<sub>2</sub>O<sub>3</sub> scale.

As expected from Fig. 1, the Ni–Al coatings dispersing Al NPs in comparison to dispersing Al MPs have the an advantage of developing a protective Al<sub>2</sub>O<sub>3</sub> scale at lower Al contents (close to 12.9 wt% for ~75 nm-sized Al NPs at 950 °C while nearly 27.6 wt.% for the Al MPs in a size range of 1–5 μm [66]). For the Ni–Al coatings with dispersion of Al MPs, homogenization heat treatment was always needed before oxidation [67, 68]. The electrodeposited NP-dispersed coatings (ENCs) have an advantage of thermally growing a protective scale of alumina or chromia, without necessity of heat treatment. However, oxidation performance of the electrodeposited MP-dispersed coatings (EMCs) benefits from homogenization heat treatment. For example, Ni-12.7Al with dispersion of ~1 μm-sized Al particles was a NiO former. After annealing in vacuum at 600 °C, the EMC formed an alumina scale with strong adhesion to the coating substrate. Consequently, the annealed EMC was even more oxidation-resistant than the arc-melted Ni<sub>3</sub>Al alloy during cyclic oxidation at 900 °C [69]. Similarly, the annealing in vacuum at 700 °C converted an EMC Ni-34Cr

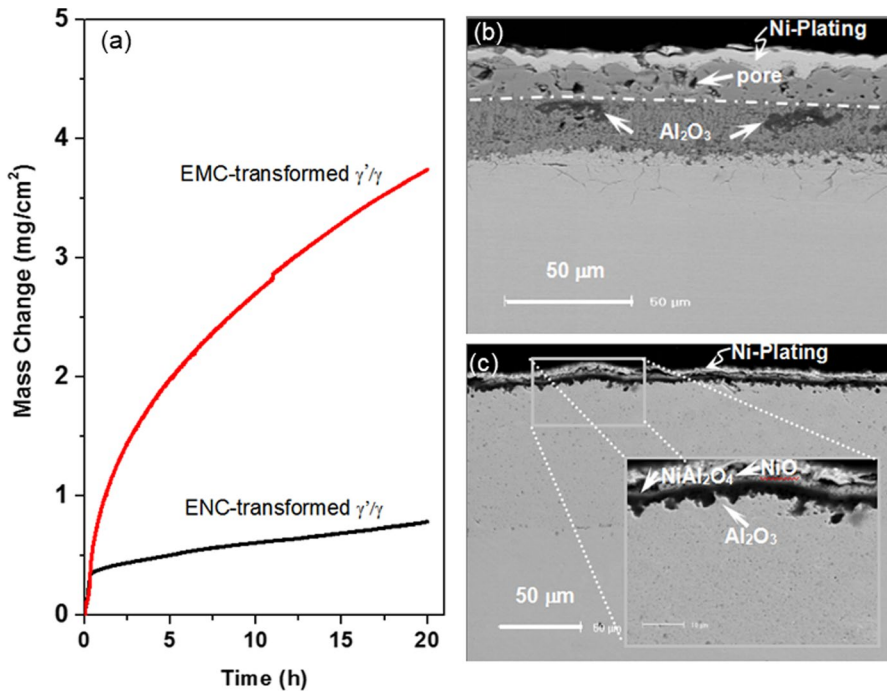


**Fig. 9** **a** Oxidation kinetics of the ENC- and EMC-transformed  $\gamma/\gamma'$  coatings and **b**, **c** cross-sectional morphologies of the oxide scales formed on the **b** EMC- and **c** ENC-transformed  $\gamma/\gamma'$  coatings for 20 h oxidation in air at 1000 °C [70]

from a NiO former to a Cr<sub>2</sub>O<sub>3</sub> former [69]. It is noticeable that the heat treatment transforms the EMC Ni–Al into novel ultrafine-grained  $\gamma/\gamma'$  dual-phase coatings. However, the EMC-transformed  $\gamma/\gamma'$  coating at 1000 °C was oxidized faster than the compositional-similar ENC-transformed counterpart, because the latter grew an alumina scale while the former still could not, as presented in Fig. 9 [70].

The Ni–Cr–Al coatings dispersing both Cr and Al NPs were also electrodeposited [23, 25, 26, 71, 72]. The ternary coatings thermally grew a protective scale of Cr<sub>2</sub>O<sub>3</sub> or Al<sub>2</sub>O<sub>3</sub>, when the amount of Cr and Al was totally over 10 wt.%. Yet, the Cr and Al amount is difficult to be further increased to a value higher than 15 wt.% by means of simple composite deposition [23, 26]. Such a low content limit undoubtedly has a negative impact on the durability of the coating at high temperatures. For this reason, a two-step method of metal (e.g. Ni, Co) electrodeposition in combination of prior electrophoretic deposition of CrAl particles has recently been proposed to develop the Ni–Cr–Al and Co–Cr–Al coatings with much higher Cr and Al contents [26, 72]. Figure 10 shows cross-sectional features of a Ni–Cr–Al coating manufactured by the two-step process [72]. Generally speaking, the CrAl particles are randomly distributed over the Ni matrix. The coating itself is compact and closely attached to the underlying metal substrate (Fig. 10a). The elemental mappings revealed that Cr and Al are homogeneously dispersed in the coating (Fig. 10b). Apparently, M–Cr–Al–Y (M=Ni, Co, or their combination) can be developed using



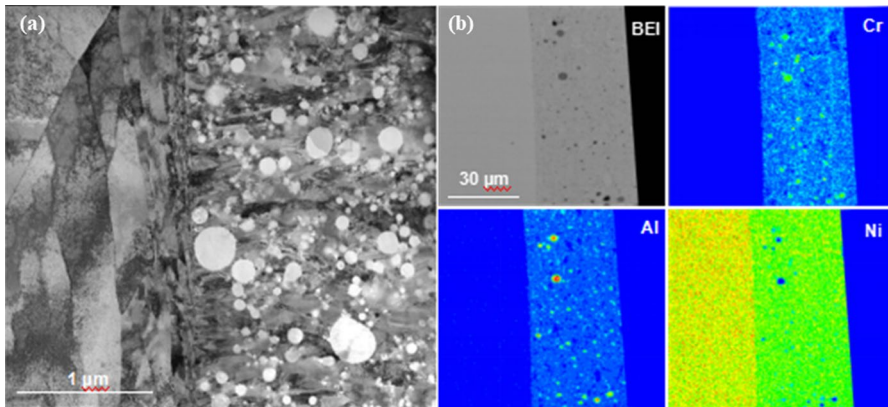


**Fig. 10** **a** TEM BF image of the cross-section of an as-deposited Ni–Cr–Al coating close to the Ni-substrate and **b** BEI and corresponding elemental X-ray mappings of the cross-sectioned NiCrAl coating [26]

metal or alloy electrodeposition, and if the CrAl particles are added with a small amount of Y, a typical element which can increase the oxidation performance of TGOs through a so-called reactive element effect (REE) [73–78]. M–Cr–Al–Y overlay coatings have been primarily developed by physical techniques [12–16, 19–22]. We applied the NPs of Cr, Al and their combinations to produce the coatings using electrochemical method.

Composite electrodeposition of M–Cr–Al–Y coatings using pre-alloyed CrAlY MPs was put forward by Foster [79, 80] and Honey [81] in 1980's. Unfortunately, since then, almost no details on the high-temperature oxidation of these coatings have been reported. To our understanding, dispersion of the MPs is difficult to make the coating oxidation-resistant, because it requires a much high particle content which is hard to reach by simple composite electrodeposition. To increase the particle content deposited, sediment co-electrodeposition was applied to prepare the Ni–Cr–Al–Y coatings [82, 83]. The method guarantees only one major surface of sample facing the particle sedimentation to have a high particle content. In addition, the M–Cr–Al–Y coatings must be heat treated before they are put into service. In contrast, the NP-dispersed M–Cr–Al–Y coatings can form a chromia- or alumina scale at much lower Cr and Al contents [23, 26]. Meanwhile, high Cr- and Al containing M–Cr–Al–Y coatings can be developed using the aforementioned two-step method. It is also convenient to regulate the ratio of the content of Cr to Al for the coating to form a protective scale of chromia or alumina as desired. The model for selective oxidation of Cr and Al of these coatings, together with their oxide maps, was reported most recently [26]. High temperature corrosion of electrodeposited M–Cr–Al–Y coatings is presented in the other article contributed to this issue [84].

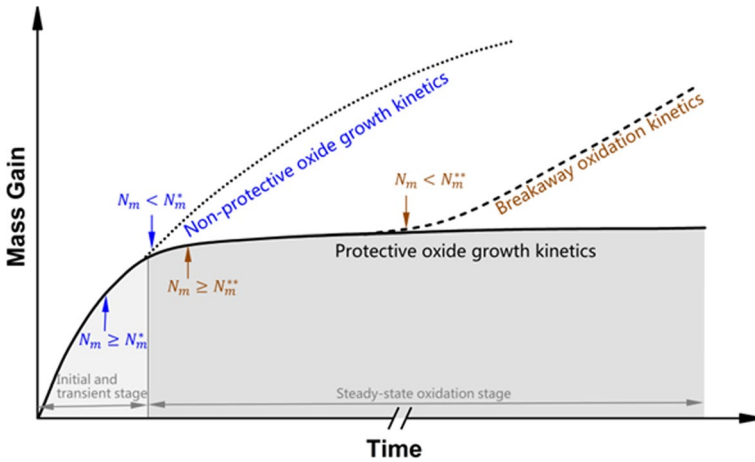


**Fig. 11** A schematic of oxidation progression of a binary alloy following various routes when the concentration of the active metal ( $N_m$ ) is (i) Smaller than  $N_m^*$  (ii) Equal or greater than both  $N_m^*$  and  $N_m^{**}$ , and (iii) less than  $N_m^{**}$  in the case that an external scale of the active metal oxide has formed during the initial and transient period

### Promoting the Selective Oxidation of Alloys

Figure 11 schematically illustrates a normal oxidation curve of a binary alloy in which the active metal exclusively grows a protective oxide scale at a high temperature. The scale occurs after an initial and transient stage, if the concentration of the active metal ( $N_m$ ) meets the requirement of Wagner’s thermodynamic condition given by Eq. (1), i.e.,  $N_m \geq N_m^*$ . Thereafter, thickening of the protective scale takes place, when  $N_m$  is not less than  $N_m^{**}$ , the critical content of the active element of the alloy. Its value can be evaluated by Wagner’s kinetic theory given by [85]

$$N_m^{**} = \frac{2V_m}{V_{ox}} \left( \frac{k_c}{D_m} \right)^{1/2} \tag{5}$$

where  $k_c$  is the parabolic rate constant for the scale growth in terms of thickness. If  $N_m < N_m^*$ , the alloy grows a non-protective scale of the noble metal oxide and its oxidation follows the dotted curve. In the case of  $N_m^* < N_m^{**}$  and that  $N_m$  decreases with time down to a value below  $N_m^*$ , breakaway oxidation emerges and the oxidation kinetics follows the dashed line. If taking a  $Cr_2O_3$ -forming alloy as an example, the value of  $N_{Cr}$  at the beginning of oxidation is undoubtedly not less than  $N_{Cr}^*$  required for thermodynamic formation of an initial continuous  $Cr_2O_3$  layer, and afterwards the value  $N_{Cr}$  is not less than  $N_{Cr}^{**}$  for kinetically maintaining the steady-state  $Cr_2O_3$  growth. For a Ni–Cr binary alloy, it is generally accepted that a minimum Cr content of 20 wt.% ( $N_{Cr}^*=0.22$ ) is required to form a continuous  $Cr_2O_3$  layer [51, 52, 86]. The calculations following Wagner’s treatment indicate that the value of  $N_{Cr}^{**}$ (0.16) predicted based on the experimental result of oxidation at 800 °C is smaller than that of  $N_{Cr}^*$  (0.24) [87]. This suggests that for a NiO-forming Ni–Cr alloy but with the Cr



content between  $N_{Cr}^*$  and  $N_{Cr}^{**}$ , it can be theoretically converted to a chromia former scale once a continuous chromia layer can form during a short and initial and transient period. The concept is detailed below.

When oxidation starts, NiO and  $Cr_2O_3$  nucleate but NiO always covers the Ni–Cr alloy surface (Fig. 1). The situation would be reversed if  $Cr_2O_3$  nucleation can be thermodynamically promoted. That copious  $Cr_2O_3$  nuclei quickly appear sharply decreases  $p_{O_2}$  at the oxidation front down to a critical value suppressing NiO growth. This promotes the linkage of the internal  $Cr_2O_3$  particles to form a continuous  $Cr_2O_3$  layer. On its basis, a methodology to catalyze  $Cr_2O_3$  nucleation by application of the NPs of a metal oxide with specific crystal structure is proposed [87]. It is known that a critical excess free energy ( $\Delta G^*$ ) is needed for the nucleation of  $Cr_2O_3$  from the alloy.  $Cr_2O_3$  has hcp structure. If the Ni–Cr alloy surface was placed in advance with a layer of NPs of hcp structured metal oxide such as  $\alpha-Al_2O_3$ . The hcp oxide NPs can act as the embryos of isostructural  $Cr_2O_3$ , energetically and crystallographically catalyzing direct epitaxial growth of the TGO.

A thin film of  $\alpha-Al_2O_3$  NPs can be added to Ni–Cr alloys by spray or electrophoretic deposition. The thin film is porous. On its basis, it is assumed that pre-setting the surface NPs does not significantly change  $N_O^S$  and  $N_O$  in Eq. (1), and consequently  $N_{Cr}^*$ . Figure 12 shows the oxidation curves of various Ni–Cr binary alloy without and with the surface dispersed  $\alpha-Al_2O_3$  NPs during isothermal oxidation in air at 800 °C [87]. Evidently for the bare Ni–Cr alloy, the oxidation rate sharply decreased when the Cr concentration was increased from 5 wt.% and 10 wt.% to 20 wt.% (Fig. 12a). The result is understandable because Ni–20Cr alloy is a  $Cr_2O_3$  former and the other two lower-Cr alloys are NiO formers. Oxidation of the latter two, particularly Ni–10Cr, was diminished remarkably after being dispersed with the  $\alpha-Al_2O_3$  NPs (Fig. 12b). Morphological observations indicated that the surface pre-setting of  $\alpha-Al_2O_3$  NPs successfully converted Ni–10Cr from a NiO former (Fig. 13a) to a  $Cr_2O_3$  former (Fig. 13b). The NiO-to- $Cr_2O_3$  transformation is consistent with our prediction that the thermal growth of  $Cr_2O_3$  on the Ni–Cr alloy can be catalyzed by  $\alpha-Al_2O_3$  NPs, because those attached to the alloy fundamentally minimize  $\Delta G^*$  for  $Cr_2O_3$  nucleation, facilitating rapid growth of  $Cr_2O_3$  around

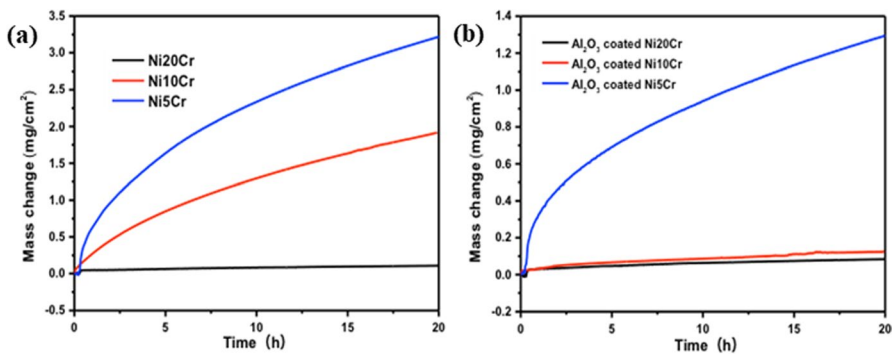


**Fig. 12** Oxidation kinetics of various Ni–Cr alloys **a** without and **b** surface dispersion of  $\alpha-Al_2O_3$  NPs in air at 800 °C [87]

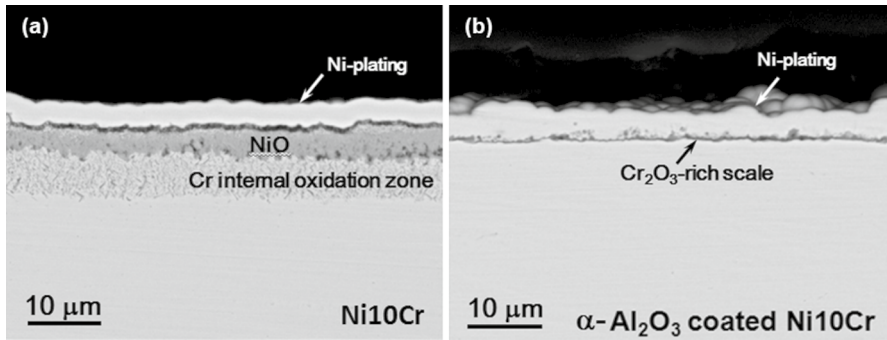


**Fig. 13** Cross-sectional BEI of the **a** bare Ni-10Cr alloy and **b**  $\alpha$ - $\text{Al}_2\text{O}_3$  NPs-coated counterpart after 20 h in air at 800 °C [87]

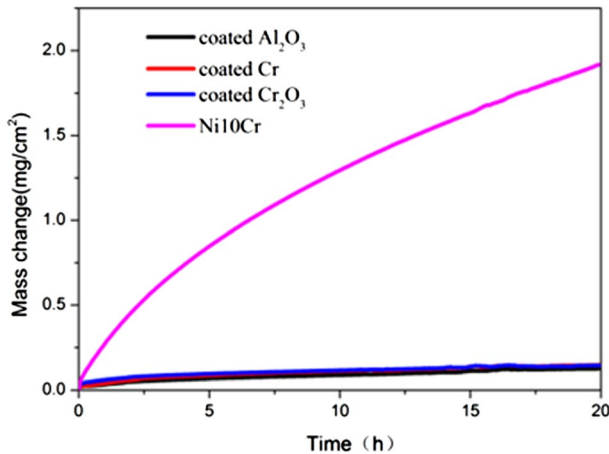


**Fig. 14** Oxidation kinetics in air at 800 °C of the Ni-10Cr alloy without and with surface dispersion of  $\alpha$ - $\text{Al}_2\text{O}_3$  or  $\text{Cr}_2\text{O}_3$  NPs

ubiquitous  $\alpha$ - $\text{Al}_2\text{O}_3$  NPs to form a continuous layer; thereafter, the  $\text{Cr}_2\text{O}_3$  layer can steadily thicken at the Cr concentration of Ni-10Cr. The surface  $\alpha$ - $\text{Al}_2\text{O}_3$  NPs also reduced the oxidation rate of Ni-5Cr; however, its Cr concentration cannot allow the  $\alpha$ - $\text{Al}_2\text{O}_3$ -catalyzed  $\text{Cr}_2\text{O}_3$  particles to form a continuous layer and then kinetically maintain its steady-state growth [87]. Apparently,  $\text{Cr}_2\text{O}_3$  NPs can play a similar role as  $\alpha$ - $\text{Al}_2\text{O}_3$  NPs in kinetically converting Ni-10Cr to a  $\text{Cr}_2\text{O}_3$  former, as presented in Fig. 14. Cr NPs can be instantaneously oxidized into *hcp*  $\text{Cr}_2\text{O}_3$ . Thus, there is no difference in catalytic effect between Cr NPs and  $\text{Cr}_2\text{O}_3$  NPs. The oxidation kinetics of the bare and  $\alpha$ - $\text{Al}_2\text{O}_3$  NPs-dispersed Ni-10Cr-5Al ternary alloy in air at 900 °C were measured (Fig. 15a). The bare alloy was oxidized faster after ~2 h. Strikingly, a low oxidation rate still remained during the time period when it was dispersed with surface  $\alpha$ - $\text{Al}_2\text{O}_3$  NPs. Cross-sectional investigation revealed that the bare alloy for 2 h oxidation mainly formed an external  $\text{Cr}_2\text{O}_3$  scale with internal  $\text{Al}_2\text{O}_3$  particles.

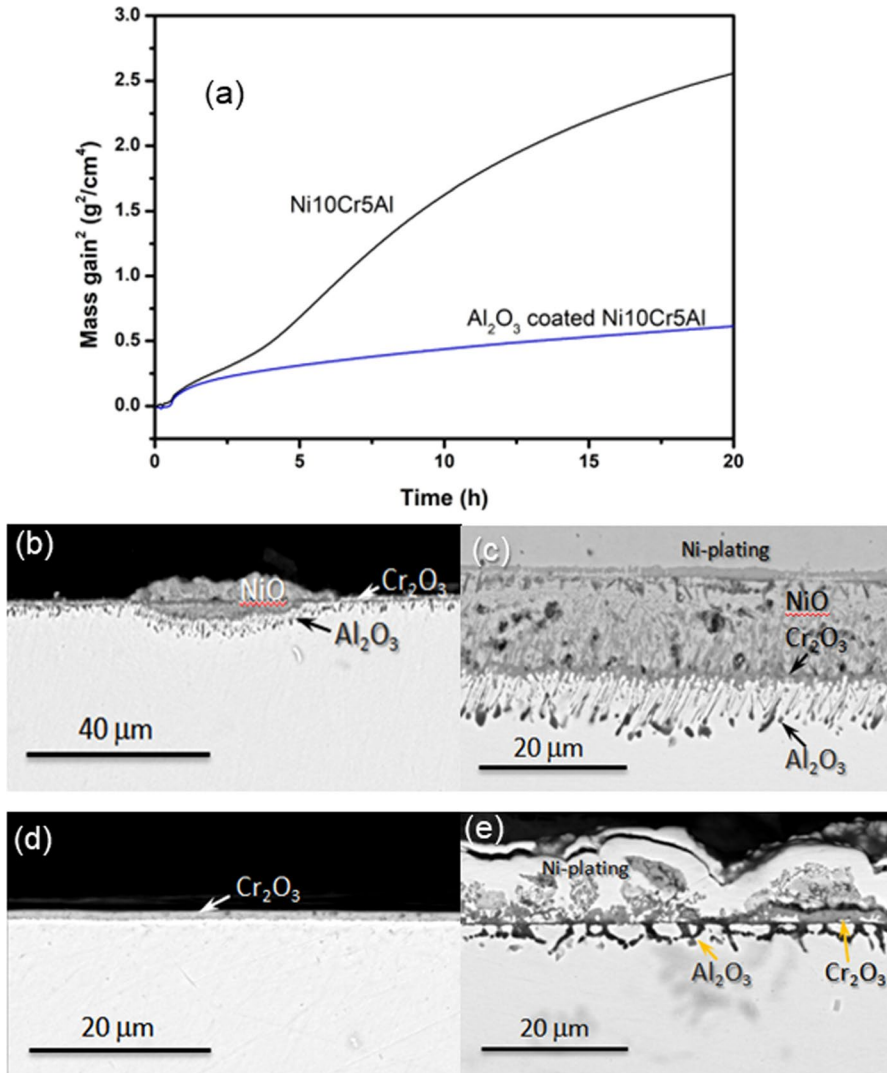


**Fig. 15** a Oxidation kinetics in air at 900 °C of an arc-melted Ni-10Cr-5Al alloy without and with surface  $\alpha$ -Al<sub>2</sub>O<sub>3</sub> NPs and b–e cross-sectional SEM morphologies of the (b, c) bare alloy and (d, e)  $\alpha$ -Al<sub>2</sub>O<sub>3</sub> NPs-coated alloy after b, d 2 h and c–e 20 h oxidation

Ni-rich oxide protuberances occurred locally (Fig. 15b). It implies that the breakaway oxidation dominated by NiO growth took place. Continuous oxidation of the bare Ni-10Cr-5Al led to the formation of a thick external oxide scale (consisting of outer NiO layer and inner Cr<sub>2</sub>O<sub>3</sub> layer) and an aluminum internal oxidation zone (Fig. 15c). The  $\alpha$ -Al<sub>2</sub>O<sub>3</sub> dispersed Ni-10Cr-5Al exclusively formed an external

Cr<sub>2</sub>O<sub>3</sub>-rich scale after 2 h oxidation (Fig. 15d). The oxide scale was dense and the underlying Al<sub>2</sub>O<sub>3</sub> TGO almost formed a continuous layer thereafter (Fig. 15e).

The result strongly supports that surface spreading of NPs of either hcp metal oxides or metals which are able to be oxidized into hcp oxides is promising to convert a non-oxidation-resistant Ni-base alloy to an oxidation-resistant one by catalyzing thermal growth of isostructural Cr<sub>2</sub>O<sub>3</sub>. The methodology can also be applied to stimulate direct growth of stable hcp  $\alpha$ -Al<sub>2</sub>O<sub>3</sub> rather than the other alumina polymorphs with different structures. This will be detailed in the next section. To date, little research on the theory and practice of applying typical NPs to promote desired selective oxidation has been reported.

## Assisting Direct Thermal Growth of $\alpha$ -alumina on Ni–Al Intermetallics

Al<sub>2</sub>O<sub>3</sub> has various lattice structures, such as  $\alpha$ ,  $\gamma$ ,  $\theta$ , and so on [88–90]. Among them, hcp  $\alpha$ -Al<sub>2</sub>O<sub>3</sub> is the most thermodynamically stable polymorph. It exhibits a thermal growth rate about one or two orders of magnitude lower than those of the  $\theta$ - or  $\gamma$ -Al<sub>2</sub>O<sub>3</sub> [91]. Therefore, for alumina-forming alloys and coatings, those with the ability of thermally growing  $\alpha$ -Al<sub>2</sub>O<sub>3</sub> at the onset of oxidation are more oxidation-resistant. Unfortunately, metastable  $\theta$ - or  $\gamma$ -Al<sub>2</sub>O<sub>3</sub> always preferentially grow before they are transformed into stable  $\alpha$ -Al<sub>2</sub>O<sub>3</sub>. This phenomenon significantly occurs when conventional M<sub>x</sub>Al<sub>y</sub> ( $M$ =Ni [91–98], Co [99] and Fe [98, 100–103]) intermetallic alloys and coatings are oxidized below 1200 °C. In addition, their oxidation can be further aggravated with a slower metastable-to-stable alumina phase transformation. A method to assist the transformation is beneficial to increase the oxidation resistance of M<sub>x</sub>Al<sub>y</sub> alloys and coatings.

It was reported that dispersing some oxides (e.g., La<sub>2</sub>O<sub>3</sub>, Y<sub>2</sub>O<sub>3</sub>, ZrO<sub>2</sub> and HfO<sub>2</sub>) into  $\beta$ -NiAl retarded the  $\theta$ -to- $\alpha$  phase transformation, whereas TiO<sub>2</sub> dispersions promoted this process [104]. The result was attributed to the difference in ionic radius of dopant cations originated from the various oxides. TiO<sub>2</sub> acted as the transformation accelerators because the ionic radius of dopant Ti<sup>4+</sup> (0.61 Å) is close to that of Al<sup>3+</sup> host ions (0.53 Å), while the inhibitors were the oxides with larger radius of cations, such as La<sub>2</sub>O<sub>3</sub> (La<sup>3+</sup>:1.06 Å), Y<sub>2</sub>O<sub>3</sub> (Y<sup>3+</sup>:0.89 Å), ZrO<sub>2</sub> (Zr<sup>4+</sup>:0.72 Å), and HfO<sub>2</sub> (Hf<sup>2+</sup>: 0.71 Å). Burtin et al. [105] proposed that the transformation kinetics depend on an annihilation reaction between anionic and cationic vacancies in which the reaction rate is correlated with the valence and ionic radius of dopant cations. Brumm and co-workers [91] found a promoted  $\theta$ -to- $\alpha$  alumina phase transformation on  $\beta$ -NiAl when it was alloyed with a certain amount of Cr, and proposed that Cr was preferentially oxidized into hcp Cr<sub>2</sub>O<sub>3</sub>, which then acted as the template for isostructural  $\alpha$ -Al<sub>2</sub>O<sub>3</sub> growth. The template effect was applied to interpret the observations of direct growth of  $\alpha$ -Al<sub>2</sub>O<sub>3</sub> on a Fe–Al alloy coated by pure films of Cr and Fe, because of their preferential oxidation into both hexagonal Cr<sub>2</sub>O<sub>3</sub> and Fe<sub>2</sub>O<sub>3</sub>[106]. Hence, we proposed that the surface dispersion of NPs of hcp metal oxide such as Cr<sub>2</sub>O<sub>3</sub> can accelerate the alumina phase transformation on M<sub>x</sub>Al<sub>y</sub> by promoting the thermal growth of  $\alpha$ -Al<sub>2</sub>O<sub>3</sub>, just as the surface  $\alpha$ -Al<sub>2</sub>O<sub>3</sub> nanodispersions promoted the Cr<sub>2</sub>O<sub>3</sub> growth on the Ni–Cr alloy as described above.

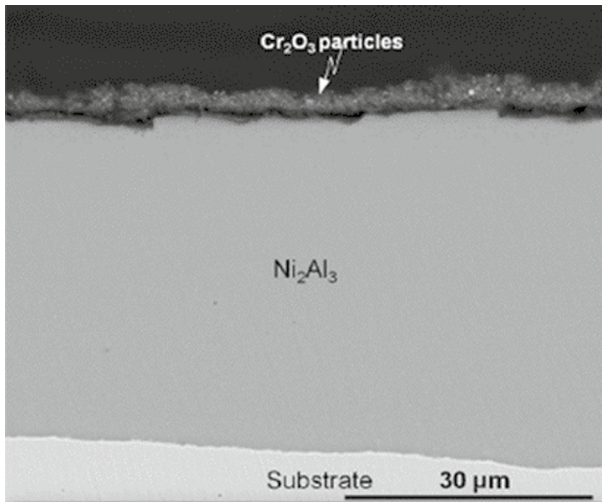


**Fig. 16** Cross-sectional SEM morphology of a Ni<sub>2</sub>Al<sub>3</sub> coating with a thin porous surface layer of Cr<sub>2</sub>O<sub>3</sub> nanoparticles [107]

Accordingly, we dispersed differently-structured metal oxide NPs onto a Ni<sub>2</sub>Al<sub>3</sub> coating by spray or electrophoretic deposition. The oxide NPs layer is thin and porous, as typically presented in Fig. 16 [107]. The nickel aluminide coating was prepared on pure nickel by pack aluminization at temperatures in a range of 600–650 °C [108, 109]). Figure 17a shows the oxidation curves of the Ni<sub>2</sub>Al<sub>3</sub> coatings without and with surface oxide nanodispersions in air at 1000 °C. There was no big difference in the oxidation rate of the bare Ni<sub>2</sub>Al<sub>3</sub> and those dispersing Y<sub>2</sub>O<sub>3</sub> and SiO<sub>2</sub> NPs. The CeO<sub>2</sub> NP dispersion decreased the oxidation rate to a certain extent. In contrast, the aluminide coating was oxidized most slowly when its surface was dispersed with NPs of Cr<sub>2</sub>O<sub>3</sub> and TiO<sub>2</sub>. For clarifying if and only if the hcp oxide dispersions assist the thermal growth of α-Al<sub>2</sub>O<sub>3</sub>, the time-dependent evolution of alumina phases on the Ni<sub>2</sub>Al<sub>3</sub> coating without and with various oxide nanodispersions was investigated using the photostimulated luminescence spectroscopy (PSLS). In a stress-free state, α-Al<sub>2</sub>O<sub>3</sub> has two characteristic luminescence lines of 14,432 and 14,402 cm<sup>-1</sup>, and θ-Al<sub>2</sub>O<sub>3</sub> has characteristic doublets of 14,645 and 14,575 cm<sup>-1</sup> [94, 110, 111]. Figure 17b indicates that for 10 min oxidation of the naked Ni<sub>2</sub>Al<sub>3</sub> coating there appear two weak θ-Al<sub>2</sub>O<sub>3</sub> lines with the frequency at 14,538.24 and 14,610.74 cm<sup>-1</sup>, respectively. The θ-Al<sub>2</sub>O<sub>3</sub> line intensities get stronger and stronger with the time increased to 30 min, 1 h and 2 h. In the meantime, two weak α-Al<sub>2</sub>O<sub>3</sub> lines occur at lower frequencies after 1 h and their intensities significantly increase with time. In particular, after 3 h, the intensities of the α-Al<sub>2</sub>O<sub>3</sub> doublet get much stronger but θ-Al<sub>2</sub>O<sub>3</sub> doublets almost disappear, suggesting that θ-Al<sub>2</sub>O<sub>3</sub> has been almost transformed into α-Al<sub>2</sub>O<sub>3</sub>. Strikingly, no θ-Al<sub>2</sub>O<sub>3</sub> spectrum has been recorded from the Cr<sub>2</sub>O<sub>3</sub> NPs-coated Ni<sub>2</sub>Al<sub>3</sub> coating during the early oxidation, as seen in Fig. 17c. It discloses that only α-Al<sub>2</sub>O<sub>3</sub> doublets appear almost from the beginning of oxidation and their intensities significantly increase with time. The result powerfully

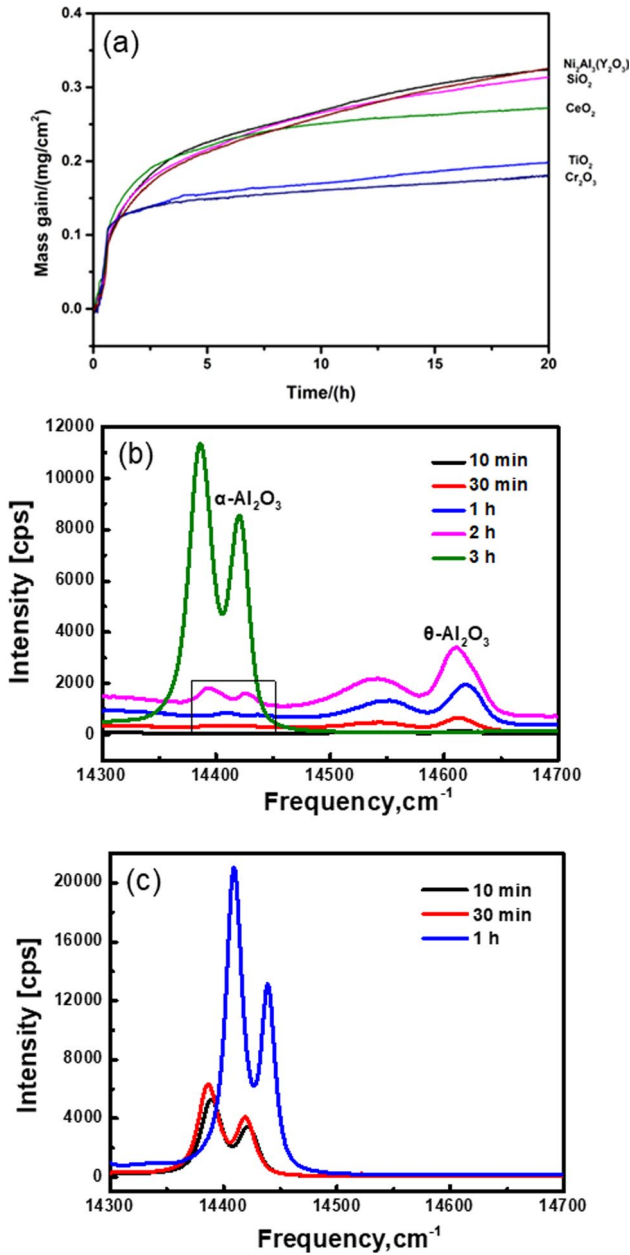


**Fig. 17** a Oxidation kinetics in air at 1000 °C of a  $\text{Ni}_2\text{Al}_3$  coating without and with various surface  $\text{Cr}_2\text{O}_3$  nanodispersions. b, c Evolution of luminescence spectrum with time recorded from the  $\text{Ni}_2\text{Al}_3$  coating b without and c with surface  $\text{Cr}_2\text{O}_3$  nanodispersions during oxidation at 1000 °C



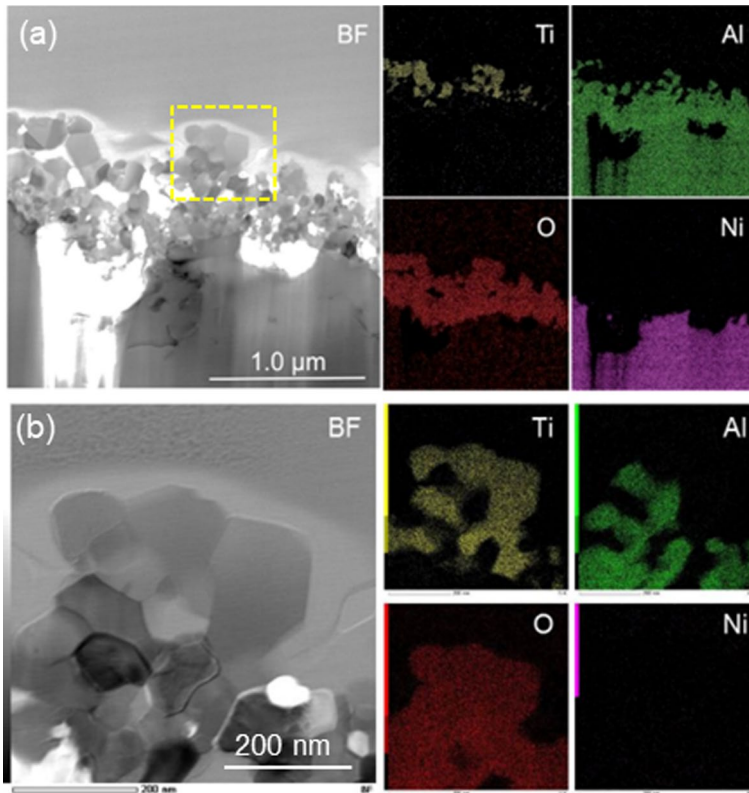


**Fig. 18** **a** TEM BF image and corresponding elemental mappings of the cross-sectioned  $\text{Ni}_2\text{Al}_3$  coating with dispersion of surface  $\text{TiO}_2$  NPs after 30 min oxidation in air at 1000 °C [113] **b** A high magnified image of the framed region in **(a)** and corresponding elemental mappings

supports that the surface  $\text{Cr}_2\text{O}_3$  nanodispersions can promote the direct thermal growth of  $\alpha\text{-Al}_2\text{O}_3$  by skipping the  $\theta$ -to- $\alpha$  transformation process. The  $\alpha\text{-Al}_2\text{O}_3$  line frequency positions shift with time, due to variation of residual compressive stresses in the alumina scale [88, 112].

The luminescence spectrum acquisition also indicates that dispersing  $\text{TiO}_2$  NPs onto the  $\text{Ni}_2\text{Al}_3$  coating promoted the direct growth of  $\alpha\text{-Al}_2\text{O}_3$  [113]. For a deeper understanding of the result, the  $\text{TiO}_2$  NPs-coated  $\text{Ni}_2\text{Al}_3$  coating after oxidation was investigated under TEM. Figure 18a shows the cross-sectional TEM bright-field (BF) image and corresponding elementary mappings of the  $\text{TiO}_2$ -coated  $\text{Ni}_2\text{Al}_3$  for 30 min oxidation in air 1000 °C. The intermetallic coating exclusively grew an alumina scale. It appears to be double-layered, consisting of an inner continuous alumina layer and an outer discontinuous alumina layer co-existed with  $\text{TiO}_2$ . A high magnified view of the framed box in the outer layer is presented in Fig. 18b. The alumina crystals are tightly attached to but separated by  $\text{TiO}_2$  NPs. The result strongly suggests that the outer alumina firstly grew around the  $\text{TiO}_2$  NPs and then filled the interparticle spacings. After that, the alumina grew inward, forming the



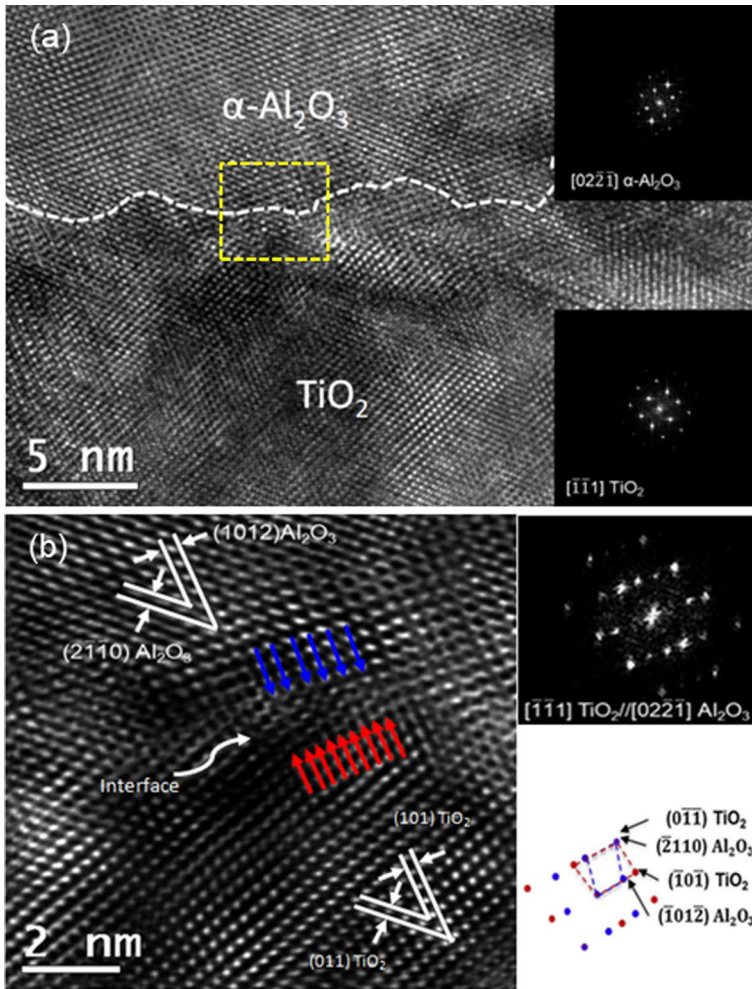


**Fig. 19** **a** HRTEM image with inserted electron diffraction patterns of a  $\text{TiO}_2$  nanoparticle attached by thermally grown  $\alpha\text{-Al}_2\text{O}_3$  after 30 min oxidation of the  $\text{TiO}_2$  NPs-treated  $\text{Ni}_2\text{Al}_3$  coating in air at 1000 °C. **b** A high magnified image with corresponding FFT and indexed patterns of the framed region in **(a)** showing the orientation relationship of the  $\alpha\text{-Al}_2\text{O}_3/\text{TiO}_2$  interface [113]

inner continuous layer. The inner and outer aluminas are both  $\alpha\text{-Al}_2\text{O}_3$  [114]. Figure 19a shows high-resolution TEM image of the  $\alpha\text{-Al}_2\text{O}_3/\text{TiO}_2$  interface and corresponding selected area electron diffraction patterns of  $\alpha\text{-Al}_2\text{O}_3$  along the  $[022\bar{1}]$  zone axis and  $\text{TiO}_2$  along the  $[\bar{1}\bar{1}1]$  zone axis. Based on the measured lattice plane spacing and angle between lattice planes along with Fourier transformation (FFT) patterns, it appears that the  $\text{TiO}_2/\alpha\text{-Al}_2\text{O}_3$  interface has specific crystalline

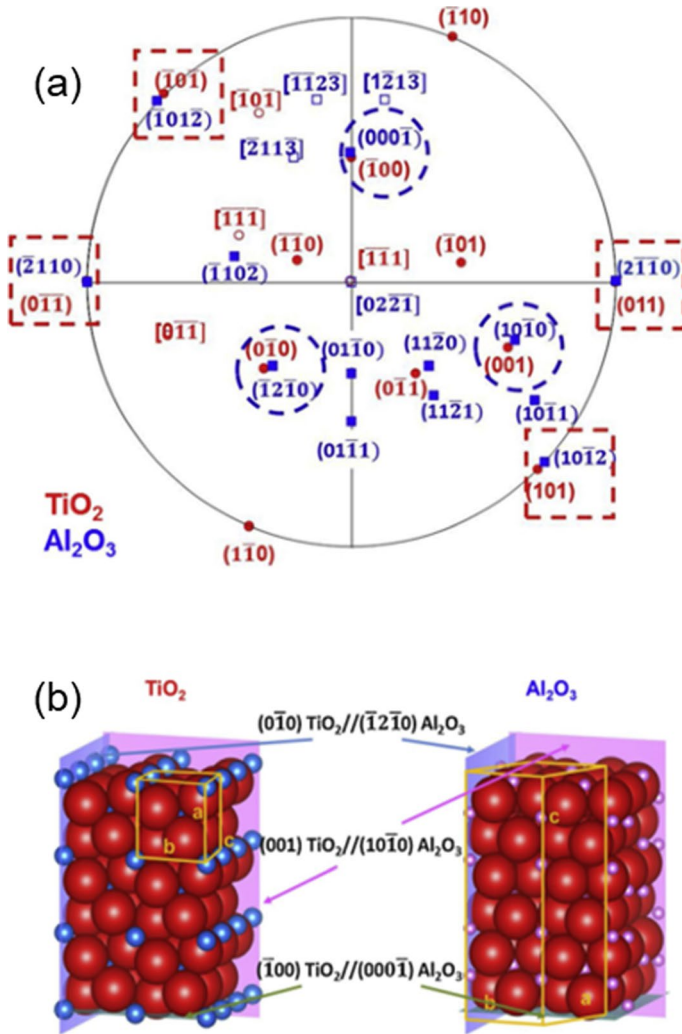


**Fig. 20** **a** Superimposed stereographic projections of  $[\bar{1}\bar{1}\bar{1}]$   $\text{TiO}_2$  and  $[02\bar{2}1]$   $\text{Al}_2\text{O}_3$ . **b** Atomic structure of  $\alpha\text{-Al}_2\text{O}_3$  and  $\text{TiO}_2$  with the ORs of  $(\bar{1}\ 00)\ \text{TiO}_2//(\bar{1}2\bar{1}\ 0)\ \text{Al}_2\text{O}_3$ ,  $(0\ \bar{1}\ 0)\ \text{TiO}_2//(\bar{1}2\bar{1}\ 0)\ \text{Al}_2\text{O}_3$  and  $(001)\ \text{TiO}_2//(\bar{1}0\ \bar{1}\ 0)\ \text{Al}_2\text{O}_3$ , where red balls represent oxygen anions while blue and pink balls represent titanium cations and aluminum cations, respectively [113] (Color figure online)

orientation relationships (ORs) of  $(101)\ \text{TiO}_2//(\bar{1}0\ \bar{1}\ 2)\ \text{Al}_2\text{O}_3$ , and  $(011)\ \text{TiO}_2//(\bar{2}\ \bar{1}\ \bar{1}\ 0)\ \text{Al}_2\text{O}_3$ , as seen in Fig. 19b [113, 114].

The superimposed stereographic projections along the zone axis  $[\bar{1}\bar{1}\bar{1}]$  of  $\text{TiO}_2$  and the zone axis  $[02\bar{2}1]$  of  $\text{Al}_2\text{O}_3$  are presented in Fig. 20a, where the  $(011)\ \text{TiO}_2$  stereographic projection is rotated around the  $[\bar{1}\bar{1}\bar{1}]$   $\text{TiO}_2$  direction to ensure a

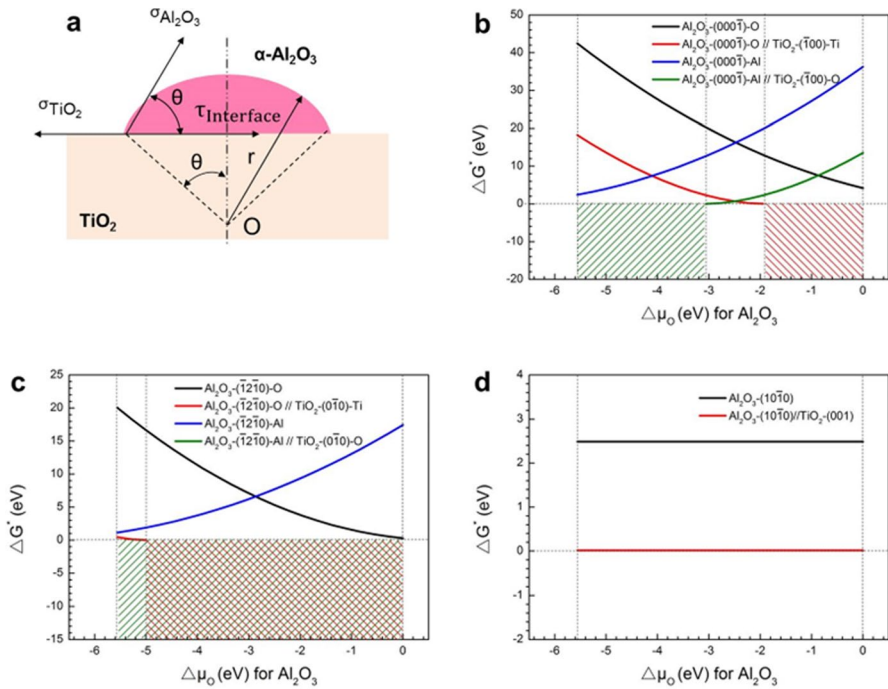


**Fig. 21** **a** Schematic heterogeneous nucleation process of  $\alpha$ -Al<sub>2</sub>O<sub>3</sub> on TiO<sub>2</sub>; **b**, **c**, **d** The calculated energy barrier  $\Delta G^*$  for nucleation of the **b** (00  $\bar{1}$  0), **c** ( $\bar{1}2\bar{1}$  0) and **d** ( $10\bar{1}$  0) planes of  $\alpha$ -Al<sub>2</sub>O<sub>3</sub> on the nickel aluminide surface (black and blue lines) and at the TiO<sub>2</sub>/nickel aluminide interface (red and green lines) [113] (Color figure online)

coincidence between the (011) TiO<sub>2</sub> and ( $2\bar{1}\bar{1}$ 0) Al<sub>2</sub>O<sub>3</sub>. Obviously, (101) TiO<sub>2</sub> and (10 $\bar{1}$ 2) Al<sub>2</sub>O<sub>3</sub> coincide at the same position with a slight deviation angle. Similarly, the two oxides have the other ORs of ( $\bar{1}$ 00) TiO<sub>2</sub>//( $000\bar{1}$ ) Al<sub>2</sub>O<sub>3</sub>, (0  $\bar{1}$ 0) TiO<sub>2</sub>//( $\bar{1}2\bar{1}$ 0) Al<sub>2</sub>O<sub>3</sub> and (001) TiO<sub>2</sub>//(10  $\bar{1}$ 0) Al<sub>2</sub>O<sub>3</sub>. The occurrence of these ORs between TiO<sub>2</sub> and Al<sub>2</sub>O<sub>3</sub> is illustrated in Fig. 20b.

The observation of the typical ORs between rutile TiO<sub>2</sub> and corundum  $\alpha$ -Al<sub>2</sub>O<sub>3</sub> can interpret why the TiO<sub>2</sub>-treated Ni<sub>2</sub>Al<sub>3</sub> coating is able to grow  $\alpha$ -Al<sub>2</sub>O<sub>3</sub> by skipping  $\theta$ -to- $\alpha$  transformation. It is known that the critical active energy ( $\Delta G_\alpha^*$ ) for the coating to homogeneously nucleate an  $\alpha$ -Al<sub>2</sub>O<sub>3</sub> sphere with a critical radius  $r^*$  can be expressed as follows:

$$\Delta G_\alpha^* = \frac{16\pi\sigma^3}{3\Delta G_v^2} \tag{6}$$

where  $\sigma$  represents the surface energy of the Al<sub>2</sub>O<sub>3</sub> sphere and  $\Delta G_v$  is the energy change to form the oxide per unit volume and always negative. Assuming  $\alpha$ -Al<sub>2</sub>O<sub>3</sub> heterogeneous nucleation on rutile TiO<sub>2</sub> to form a spherical cap with the wetting angle  $\theta$  as illustrated in Fig. 21a,  $\Delta G_\alpha^*$  can be expressed as [113],

$$\Delta G_{\alpha}^{*} = \frac{16\pi\sigma^3}{3\Delta G_v^2} \left( \frac{2 - 3\cos\theta + \cos^3\theta}{4} \right) \quad (7)$$

and

$$\cos = \frac{\sigma_{\text{TiO}_2} - \tau_{\text{interface}}}{\sigma_{\text{Al}_2\text{O}_3}} \quad (8)$$

where  $\sigma_{\text{Al}_2\text{O}_3}$  and  $\sigma_{\text{TiO}_2}$  are the surface energy of the related oxides, respectively.  $\tau_{\text{interface}}$  is the  $\alpha\text{-Al}_2\text{O}_3/\text{TiO}_2$  interface energy.  $\sigma_{\text{Al}_2\text{O}_3}$  and  $\sigma_{\text{TiO}_2}$  is a function of oxygen chemical potential. Accordingly,  $\Delta G^*$  for the  $\alpha\text{-Al}_2\text{O}_3$  formation on the bare and  $\text{TiO}_2$  NPs-coated  $\text{Ni}_2\text{Al}_3$  covered can be calculated by Eqs. (3) and (7), in which  $\sigma_{\text{TiO}_2}$ ,  $\sigma_{\text{Al}_2\text{O}_3}$  and  $\tau_{\text{interface}}$  can be obtainable by first-principles calculation [113, 114]. Figure 21(b–d) shows the calculated  $\Delta G_{\alpha}^{*}$  for nucleation of the observed (00 01), (12̄1 0) and (101 0) planes of  $\alpha\text{-Al}_2\text{O}_3$  on the  $\text{Ni}_2\text{Al}_3$  surface (black and blue lines) and at the  $\text{TiO}_2/\text{Ni}_2\text{Al}_3$  interface but correspondingly on the  $\text{TiO}_2$  (1̄00), (0 1̄0) and (001) planes (red and green lines). Both (00 01) (Fig. 21b) and (12̄1 0) (Fig. 21c) surfaces of  $\alpha\text{-Al}_2\text{O}_3$  exhibit two different terminations, i.e., O termination (black and red curves) and Al termination (blue and green curves), whereas its (101 0) surface only has one kind of termination (Fig. 21d). As is evident,  $\Delta G_{\alpha}^{*}$  becomes negative in a blue- and red-shadowed region, when the variation of chemical potential of oxygen ( $\Delta\mu_o$ ) from  $-5.56$  to  $-3.06$  eV and from  $-1.95$  to  $0$  eV, implying that the (00 01) plane of  $\alpha\text{-Al}_2\text{O}_3$  nucleates and spreads out on either the entire O termination or Ti termination of the  $\text{TiO}_2$  (1̄00) surface (Fig. 21b). Similarly, the (12̄1 0) plane of  $\alpha\text{-Al}_2\text{O}_3$  prefers to nucleate on the O-terminated  $\text{TiO}_2$  (1̄00) plane at  $\Delta\mu_o$  ranging from  $-5.56$  to  $0$  eV and on the Ti-terminated  $\text{TiO}_2$  (1̄00) plane at any  $\Delta\mu_o$  above  $-5.00$  eV (Fig. 21b). The (10 1̄0) plane of  $\alpha\text{-Al}_2\text{O}_3$  can even spontaneously nucleate along the O close-packed direction on the  $\text{TiO}_2$  (001) plane because  $\Delta G_{\alpha}^{*}$  is a  $\Delta\mu_o$ -independent zero constant (Fig. 21d). The calculations indicate that  $\Delta G_{\alpha}^{*} \leq 0$  can be achieved for the nucleation of  $\alpha\text{-Al}_2\text{O}_3$  on the  $\text{TiO}_2$  NPs along specific orientations of the rutile oxide. In other words, dispersing  $\text{TiO}_2$  NPs onto the nickel aluminate can thermodynamically promote  $\alpha\text{-Al}_2\text{O}_3$  direct growth. The result highlights the significance of the oxygen sublattice structure of the rutile oxide for the template effect on the corundum oxide formation.

Based on the above result, it is understandable why  $\text{M}_x\text{Al}_y$  preferentially grow  $\theta\text{-Al}_2\text{O}_3$  rather than  $\alpha\text{-Al}_2\text{O}_3$ . This is schematically elucidated in Fig. 22. The energy barrier  $\Delta G_{\alpha}^{*}$  for direct  $\alpha\text{-Al}_2\text{O}_3$  nucleation (Case I) is larger than  $\Delta G_{\theta}^{*}$  for  $\theta\text{-Al}_2\text{O}_3$  nucleation. Accordingly,  $\theta\text{-Al}_2\text{O}_3$  always grows in advance at the beginning of oxidation (Case II). Accompanying this process,  $\alpha\text{-Al}_2\text{O}_3$  gradually occurs through phase transformation of  $\theta\text{-Al}_2\text{O}_3$  at the oxide/ $\text{M}_x\text{Al}_y$  interface. The energy barrier  $\Delta G_{\theta\rightarrow\alpha}^{*}$  for the “ $\theta$ -to- $\alpha$ ” transformation to form  $\alpha\text{-Al}_2\text{O}_3$  is lower. Because  $\theta\text{-Al}_2\text{O}_3$  has a face-centered cubic (fcc) structure of oxygen sublattices and  $\alpha\text{-Al}_2\text{O}_3$  has a hcp oxygen sublattice, with 2/3 of the octahedral interstices filled with aluminum cations, the  $\theta$ -to- $\alpha$  transformation may follow a “synchro-shear” model. It was firstly proposed by Kachi et al. in study of the transformation of  $\gamma\text{-Fe}_2\text{O}_3$  to  $\alpha\text{-Fe}_2\text{O}_3$  during the dehydration process of  $\text{FeOOH}$  [114]. The

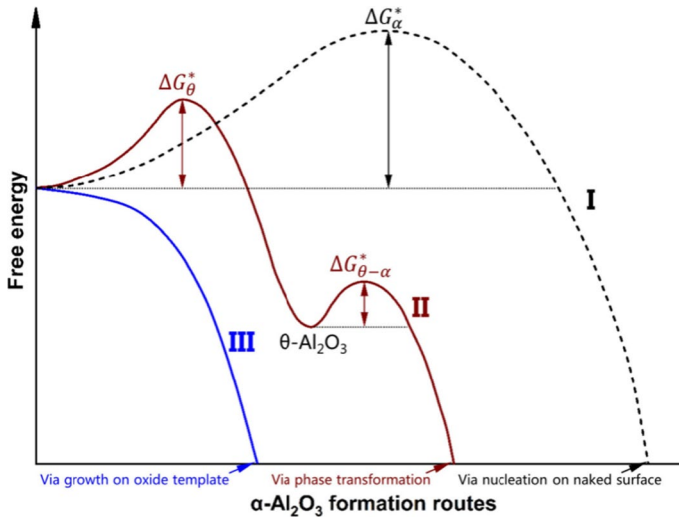


**Fig. 22** Schematic active energy required for the formation of  $\alpha$ - $\text{Al}_2\text{O}_3$  on a nickel aluminide in assumed cases: (i) Direct growth of  $\alpha$ - $\text{Al}_2\text{O}_3$ , (ii)  $\alpha$ - $\text{Al}_2\text{O}_3$  formation resulted from  $\theta$ - $\text{Al}_2\text{O}_3$  transformation, and (iii) Direct growth of  $\alpha$ - $\text{Al}_2\text{O}_3$  on template of dispersed NPs of metal oxide with either *hcp* structure or *hcp* O sublattice structure

“synchro-shear” model is a two-step process. The first step is a martensitic transformation process, in which a series of shear displacement causes a conversion of the oxygen sublattice from fcc to *hcp* structure. The second step is an almost simultaneous diffusion process, in which the Al cations migrate to fill the empty honeycomb octahedral interstices sites ( $\text{O}_h$ ). The first-principle calculation indicates that  $\theta$ - $\text{Al}_2\text{O}_3$  seed with a critical size of above 22 nm is in need for the formation of a stable  $\alpha$ - $\text{Al}_2\text{O}_3$  embryo ahead of the alumina phase transformation [115]. Afterward, the oxidation temperature and oxygen potential offer the energy enough to drive the migration Al cations to the appropriate empty  $\text{O}_h$  sublattice. When  $\text{M}_x\text{Al}_y$  is dispersed with NPs of metal oxide with either *hcp* structure or *hcp* O sublattice structure (Case III), these oxide NPs exert “template” effect catalyzing the direct growth of corundum  $\alpha$ - $\text{Al}_2\text{O}_3$ . Taking rutile  $\text{TiO}_2$  as an example, the oxide and  $\alpha$ - $\text{Al}_2\text{O}_3$  share the well-matching oxygen sublattice. Thus,  $\alpha$ - $\text{Al}_2\text{O}_3$  stable embryo can be energetically allowable to form around  $\text{TiO}_2$  NPs without necessity of shear displacement, just simply through layer-by-layer stacking of O anions following the *hcp* O sublattice structure of  $\text{TiO}_2$  on the aforementioned planes and rearranging of  $\text{Al}^{3+}$  at  $\text{O}_h$  to form a “honey comb” lattice structure by the cations diffusion. The  $\alpha$ - $\text{Al}_2\text{O}_3$  embryos occur at the point of contact between  $\text{TiO}_2$  NPs and the aluminide. The oxide embryos then grow in size around the NPs and finally fill the spacings among them (Fig. 18).

Direct  $\alpha$ - $\text{Al}_2\text{O}_3$  growth led to a profound enhancement of oxidation resistance of the  $\text{Cr}_2\text{O}_3$  and  $\text{TiO}_2$  NPs-coated  $\text{Ni}_2\text{Al}_3$  coating [107, 113]. The results are reflected in three aspects: (i) A noticeable decrease in oxidation rate, (ii) A slower degradation of  $\delta$ - $\text{Ni}_2\text{Al}_3$  to  $\beta$ - $\text{NiAl}$  and  $\gamma'$ - $\text{Ni}_3\text{Al}$ , and (iii) Formation of a more adherent

alumina scale. For the naked  $\text{Ni}_2\text{Al}_3$  coating oxidized at 1000 °C, large cavities occurred below the alumina scale with the  $\theta$ -to- $\alpha$  transformation. The cavities were formed by the condensation of vacancies, which were injected from the growing alumina scale for counterbalancing the outward Al cation diffusion or resulted from the metal because of Kirkendall effect pertinent to the relative diffusion rate of Ni to Al in the Al-depleted layer of the coating [108]. In contrast, no interfacial cavities were seen in the case that the  $\text{Ni}_2\text{Al}_3$  coating was treated by the surface  $\text{TiO}_2$  and  $\text{Cr}_2\text{O}_3$  NPs [107, 113].

Recent work showed that the  $\text{Ni}_2\text{Al}_3$  coating could be internally dispersed with  $\text{Cr}_2\text{O}_3$  NPs using a two-step method of Ni and  $\text{Cr}_2\text{O}_3$  NPs composite electrodeposition and aluminization at a designed temperature at which the nickel aluminide grew inwardly [116]. The internal  $\text{Cr}_2\text{O}_3$  nanodispersions caused the  $\text{Ni}_2\text{Al}_3$  coating to have a faster  $\theta$ -to- $\alpha$  transformation rate and consequently a lower oxidation rate. In addition, dispersing hcp oxides NPs with respect to their micron-sized counterparts is more effective in promoting the alumina phase transformation. The transformation appears to be somewhat faster when the internal dispersions of  $\text{Cr}_2\text{O}_3$  NPs are replaced by those of more thermodynamically stable  $\alpha\text{-Al}_2\text{O}_3$  NPs [117]. Internal  $\text{TiO}_2$  nano-dispersions also promoted the  $\theta$ -to- $\alpha$  transformation on the  $\text{Ni}_2\text{Al}_3$  coating. Due to that the internal dispersions of these oxide NPs cannot assist the direct  $\alpha\text{-Al}_2\text{O}_3$  growth, their beneficial effects on oxidation as addressed above are not significant as those presented by these oxide NPs coated on the surface [118].

## Increasing the Oxidation Resistance of Thermally-Grown Oxides

Addition of reactive element (RE), such as Y, Ce, La, or their oxides ( $\text{RE}_x\text{O}_y$ ), can improve the oxidation resistance of metals. The phenomenon was first found in 1937 by Pfeil [119]. It has been referred to as “reactive element effect” (REE) which has been reviewed in [73–78]. Various commercial alloys with  $\text{RE}_x\text{O}_y$  dispersions have been developed. For instances, high-temperature creep-resistant Inconel MA754 by mechanical alloying is a chromia-forming ODS nickel-based alloy with yttria dispersions [120, 121]. Incoloy MA 956 is an alumina-forming yttria-dispersed ODS iron-base alloy [122, 123], so is PM 2000 manufactured by powder metallurgy [124]. PM 1000 is yttria-strengthened nickel-base ODS alloy [125]. REE can be simply classified into two major categories from kinetic and mechanical aspects: a reduction in oxidation and an enhancement in scale adhesion.

One mechanistic interpretation on kinetic REE is that RE ions segregate to TGO GBs and consequently “short-circuit” diffusion of species (particularly cations) for oxide growth is blocked. RE segregation at GBs in TGOs has been discovered and validated by many investigators using TEM in combination of X-ray energy dispersive spectroscopy (EDS) [93, 126–130]. However,  $\text{RE}_x\text{O}_y$  like yttria in ODS alloys are in general more thermodynamically stable than chromia- or alumina TGO. The oxygen concentration in alloys should be not too far below the equilibrium value for Cr or Al oxidation at the TGO/alloy interface. In other word, the oxygen concentration in ODS alloys is plausibly not low enough to drive yttria dispersion to decompose and release RE ions which then diffuse toward the interface. In this case,



a question arises: How does the more stable  $RE_xO_y$  in alloys produce RE ions segregated to TGO GBs?

Peng et al. [131, 132] found that although dispersing  $La_2O_3$  particles into electrodeposited Ni film decreased its isothermal and cyclic oxidation rates at high temperatures. After 100 h thermal cycling at 1000 °C,  $La_2O_3$  particles only appeared in the outer part of the total ~50  $\mu\text{m}$ -thick NiO scale with a thickness matching the original ~30  $\mu\text{m}$ -thick Ni- $La_2O_3$  film [131]. Because of a limited solubility in NiO lattice [133, 134],  $La_2O_3$  particles in the Ni film can be regarded as inert markers. The fact that  $La_2O_3$  particles were dispersed only in the outer NiO layer symbolized that the NiO growth converted from conventional  $Ni^{2+}$  outward diffusion-dominated mechanism [135–138] to  $O^{2-}$  inward diffusion-controlled one. If the NiO growth mechanism change results from  $La_2O_3$  incorporation-induced  $p_{O_2}$  decrease at the formed NiO/Ni film interface, it is anticipated that the oxidation rate of the Ni- $La_2O_3$  film decreases with increasing  $La_2O_3$  content. Unexpectedly, the  $La_2O_3$  content increase was not certain to decrease NiO thickening rate [132]. The commercial  $La_2O_3$  particles were several micrometers in size but there existed  $La_2O_3$  nanodispersions below 5 nm in the Ni- $La_2O_3$  film [131]. Based on the results, a nanosize effect of  $La_2O_3$  dispersion on NiO kinetic growth was proposed [131, 132]. Considering the dependence of thermodynamic stability of particles on dimension: the smaller the  $La_2O_3$  particle, the larger the particle surface energy, and the weaker the  $La_2O_3$  bonds at the particle surface. When  $La_2O_3$  particle size added is so small that it is only a few nanometers, the particle surface energy would be high enough to drive the oxide to decompose, producing  $La^{3+}$  ions of a certain amount which are doped into the NiO scale. In view of the high radius ratio of  $La^{3+}$  to  $Ni^{2+}$  (1.54), the elastic energy of NiO lattice with  $La^{3+}$  doping is increased. Under the driving force of lattice misfit strain  $La^{3+}$  ions in NiO lattice segregated to the oxide GBs, where  $La^{3+}$  ions block the dominant short-circuit diffusion of  $Ni^{2+}$  cations for NiO growth.

The nanosize effect also occurred on the  $RE_xO_y$  NPs-dispersed ODS-type coatings developed by the above-mentioned two-step method [116]. The internal  $CeO_2$  nanodispersions (~7 nm in size) enhanced not only the oxidation resistance in either wet air [139] or simulated coal-combustion gasses [140] but also the erosion-oxidation resistance in a laboratory-scale fluidized-bed combustor [141] of a chromized coating prepared by pack cementation at 1120 °C. They reduced the oxidation kinetics at 700 °C of a low-temperature chromized coating [142]. Similar result was found on the low-temperature aluminized coating in the presence of the  $CeO_2$  NPs [108, 143]. Based on these publications [131, 132, 139–143],  $RE_xO_y$  nanodispersions are beneficial to kinetically reduce the growth rate of TGOs, through the popular TGO GB segregation model of RE ions, which might be produced after  $RE_xO_y$  nanodispersions have been swept over by inward growth of TGOs.

The feature with characteristic of inward growth of alumina TGO clearly appeared during oxidation of a  $CeO_2$  NPs-dispersed  $Ni_2Al_3$  coating in air at 1100 °C [144]. Figure 23a shows a cross-sectional scanning TEM (STEM) image and corresponding elementary mappings of the TGO formed for 5 min oxidation, revealing that a  $CeO_2$  NP (as arrowed) has been swept over by inward growing alumina. The TGO inward growth took place ubiquitously from a SEM view of the cross-sectioned coating for 30 min oxidation presented in Fig. 23b. The formed alumina scale



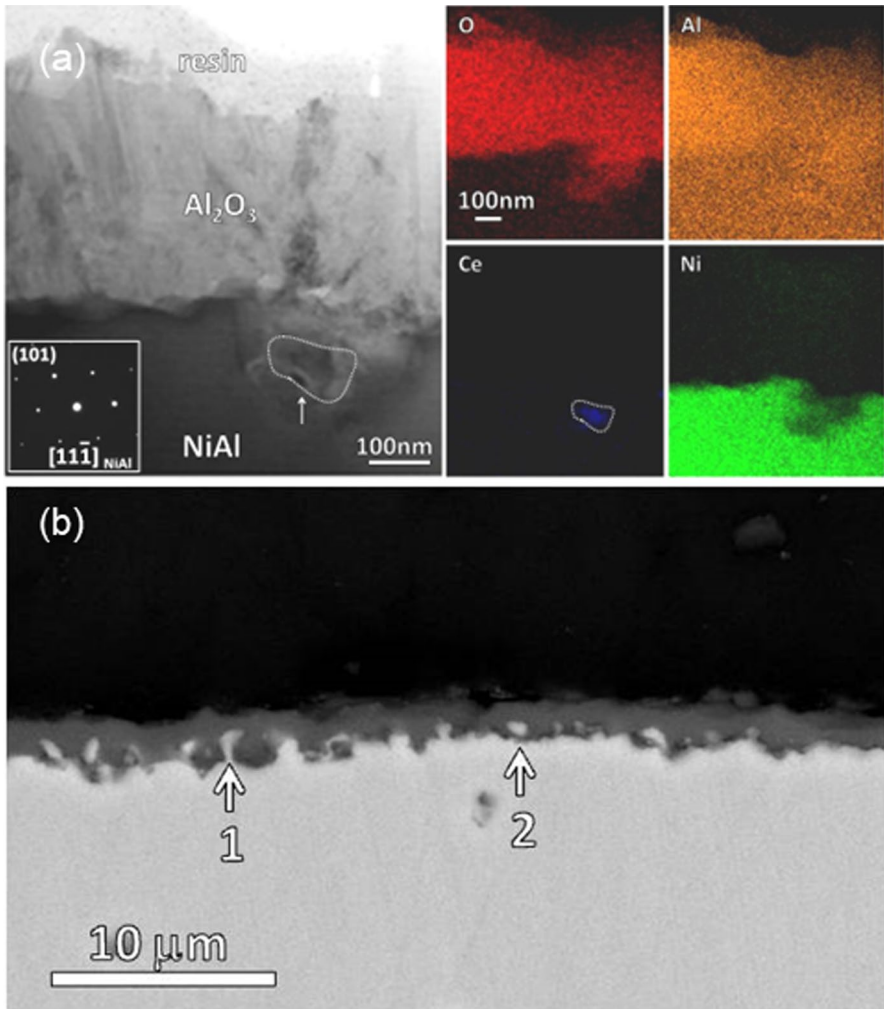


**Fig. 23** **a** STEM image and corresponding elementary mappings of the alumina scale formed on the  $\text{CeO}_2$  NPs-dispersed  $\text{Ni}_2\text{Al}_3$  coating for 5 min oxidation ( $\text{Ni}_2\text{Al}_3$  has been degraded to  $\text{NiAl}$  phase) and **b** cross-sectional SEM morphology of the alumina scale formed for 30 min oxidation in air at 1100 °C [144]

was double-layered, consisting of an inner  $\alpha\text{-Al}_2\text{O}_3$  layer and outer layer of needle-like  $\gamma\text{-Al}_2\text{O}_3$  platelets containing a high density of lamellar nanotwins (Fig. 24). The growth of  $\gamma\text{-Al}_2\text{O}_3$  platelets is controlled by aluminum cations outward diffusion along the twin boundaries (TBs), while the  $\alpha\text{-Al}_2\text{O}_3$  growth is controlled by oxygen anions inward diffusion. Elementary Ce was not detected at the coating's GBs close to  $\text{CeO}_2$  nanodispersions by EDS detector under the TEM system [144].  $\text{CeO}_2$  NPs were trapped in the alumina scale due to  $\alpha\text{-Al}_2\text{O}_3$  inward growth. HRTEM characterization revealed that the Ce-bearing oxide NPs in the inner  $\alpha\text{-Al}_2\text{O}_3$  layer was

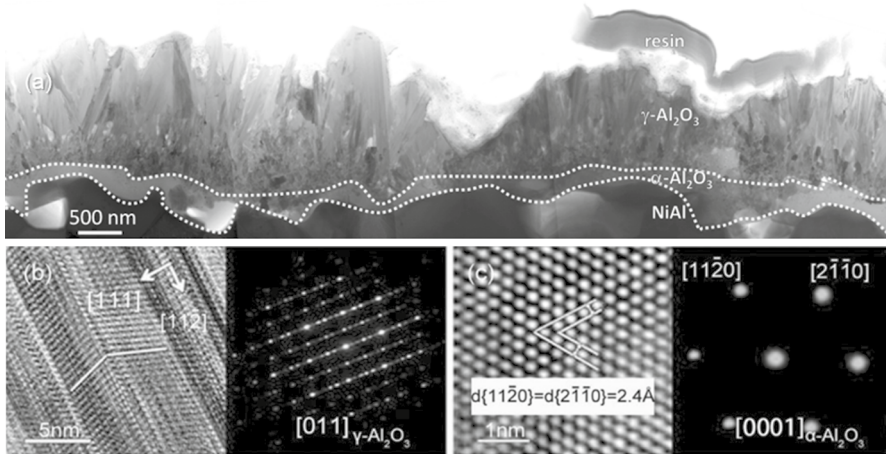


**Fig. 24** **a** Cross-sectional TEM overview of the alumina scale on the CeO<sub>2</sub> NPs-dispersed Ni<sub>2</sub>Al<sub>3</sub> coating for 30 min in air at 1100 °C; **b**, **c** HRTEM images and corresponding selected area electron diffraction patterns of **(b)** outer  $\gamma$ -Al<sub>2</sub>O<sub>3</sub> and inner  $\alpha$ -Al<sub>2</sub>O<sub>3</sub> layer, respectively [144]

CeO<sub>2</sub> while in the outer  $\gamma$ -Al<sub>2</sub>O<sub>3</sub> layer was Ce<sub>2</sub>O<sub>3</sub> (see Fig. 4 in [144]). On its basis, the CeO<sub>2</sub> NPs effect on oxidation was proposed as follows [144]. The ceria NPs, after entering the  $\alpha$ -Al<sub>2</sub>O<sub>3</sub> layer, partially decomposed, producing Ce<sup>4+</sup>. The incorporation of larger cations generated additional microstrains in the  $\alpha$ -Al<sub>2</sub>O<sub>3</sub> lattice which drove Ce<sup>4+</sup> to segregate to the oxide GBs as seen in Fig. 25. The Ce segregation at the  $\alpha$ -Al<sub>2</sub>O<sub>3</sub> GBs can be evidenced by STEM in combination of high-angle annular detector dark-field (HAADF). The Ce segregated GBs in the HAADF image appeared as the lines with a light contrast similar to that of the CeO<sub>2</sub> NPs (as arrowed in the STEM-BF image), because Ce has a higher atomic number than Al. The EDS analysis indicates the GBs containing a mean content of ~0.4 at. % Ce. Owing to the oxygen potential difference between the gas/TGO interface and the TGO/coating interface, the segregated Ce<sup>4+</sup> migrated outward along the GBs from the inner  $\alpha$ -Al<sub>2</sub>O<sub>3</sub> to the outer  $\gamma$ -Al<sub>2</sub>O<sub>3</sub>; in the meantime, Ce<sup>4+</sup> ion trapped an free electron in the n-type  $\alpha$ -Al<sub>2</sub>O<sub>3</sub> to transform to Ce<sup>3+</sup> in the p-type  $\gamma$ -Al<sub>2</sub>O<sub>3</sub>. The Ce<sup>3+</sup> there preferred to diffuse outward along the twin boundaries (TBs), causing Ce<sub>2</sub>O<sub>3</sub> to be precipitated and elongated at the TBs along the growth direction of the  $\gamma$ -Al<sub>2</sub>O<sub>3</sub> platelets. This is the reason for the observation of new rod-shaped Ce<sub>2</sub>O<sub>3</sub> nano-precipitates in the near surface area of outer  $\gamma$ -Al<sub>2</sub>O<sub>3</sub> layer (Fig. 26). That novel RE<sub>x</sub>O<sub>y</sub> particles occurred on or near the surface of the TGOs on the ODS-type alloys and coatings oxidized at high temperatures were reported elsewhere [58, 143, 145]. This confirms that the RE segregants at the GBs are not static; they can transport outward along TGO's GBs driven by the oxygen potential (i.e., oxygen chemical activity) gradient across the oxide scale [145].

The kinetic growth of alumina scale was controlled by the thickening rate of  $\gamma$ - or  $\theta$ -Al<sub>2</sub>O<sub>3</sub> in it during the early stage and then controlled by inner  $\alpha$ -Al<sub>2</sub>O<sub>3</sub> after it formed a continuous layer. Meta-stable alumina growth was dominated by outward diffusion of aluminum cations while  $\alpha$ -Al<sub>2</sub>O<sub>3</sub> growth dominated by inward diffusion

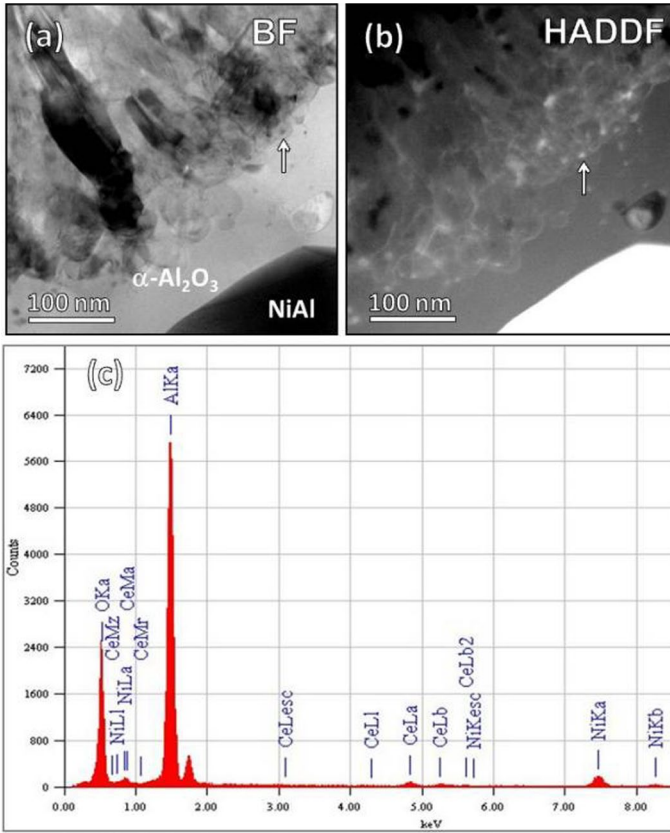


**Fig. 25** **a** STEM BF and **b** HADDF image of the  $\alpha$ -Al<sub>2</sub>O<sub>3</sub> layer with lighter GBs as a result of segregation of heavier Ce, which was confirmed by EDS analysis in (c) [144]

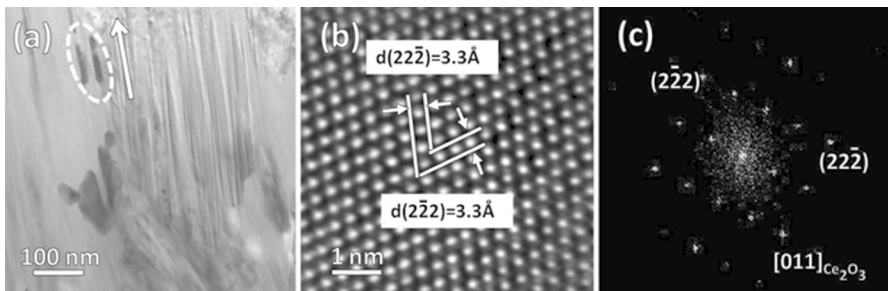


**Fig. 26** **a** TEM image of the Ce-rich oxide particles formed in the near surface area of outer  $\gamma$ -Al<sub>2</sub>O<sub>3</sub> layer; **b** HRTEM image and **c** corresponding FFT diffraction pattern identifying the framed particle as Ce<sub>2</sub>O<sub>3</sub> [144]

of oxygen anions. Thus, it was proposed that the CeO<sub>2</sub> NPs took significant effect on the alumina scaling kinetics only during the early stage, during which the outward migration of cerium cations segregated at the TGO GBs suppressed the Al<sup>3+</sup> outward diffusion for the meta-stable alumina growth [143, 144]. The CeO<sub>2</sub> REE on the alumina scale growth became not significant after the establishment of the continuous  $\alpha$ -Al<sub>2</sub>O<sub>3</sub> layer, because the stable alumina grows 1 or 2 orders of magnitude slower than the meta-stable aluminas. This explained the difference in the oxidation curves between the Ni<sub>2</sub>Al<sub>3</sub> coatings without and with CeO<sub>2</sub> nanodispersions [143].

Therefore, the size of RE<sub>x</sub>O<sub>y</sub> dispersions is a crucial parameter for them to take the REE on TGO growth. From nucleation theory, RE<sub>x</sub>O<sub>y</sub> particle with a size only above a critical size  $r^*$  is thermodynamically stable. In other words, it is not stable at a high temperature for the RE<sub>x</sub>O<sub>y</sub> dispersion with a size as small as a few nanometers as applied in our previous works. These small-sized nanodispersions are easy to decompose to release RE ions [131, 132, 139–144]. This is the prerequisite for RE<sub>x</sub>O<sub>y</sub> addition to decrease the oxidation rate of alloys and coating through the above oxide GB segregation model. On its basis, it is assumed that the oxidation performance of the alloys and coatings would benefit from dispersion of a-few-nanometer sized RE<sub>x</sub>O<sub>y</sub> NPs. RE<sub>x</sub>O<sub>y</sub> in metals are the preferential sites for annihilation and condensation of cation vacancies and “Kirkendall” vacancies. The former are injected from growing TGO and the latter result from the difference in the diffusivity of the TGO-forming element relative to the other alloying elements which cannot be thermodynamically oxidized. Uniform dispersion of small-sized RE<sub>x</sub>O<sub>y</sub> NPs tends to cause alloys and coating to thermally grow more adherent TGOs [108].

## Summary and Concluding Remarks

Nanoparticles of Cr, Al and their combinations can be applied to develop nanocomposite-type coatings such as Ni–Cr, Ni–Al, Cu–Ni–Cr and M–Cr–Al (M = Ni, Co, CoNi, et al.). These coatings have the merits of thermally growing a protective scale of chromia or alumina at a critical content of Cr or Al lower than normal level required by conventional binary or ternary alloys. When oxidation starts, the metallic NPs act as diffusionless nucleation sites of chromia or/and alumina. Numerous chromia or/and alumina particles promptly emerged, sharply decreasing  $p_{O_2}$  at the oxidation front to a threshold suppressing oxidation of noble metals of the coatings on one hand; on the other hand, nanoscale interparticle spacing makes it easier the linkage of the chromia or alumina particles through their lateral growth.

The hcp metal oxide NPs on the surface act as template seeds of an alloy containing Cr or/and Al thermally growing Cr<sub>2</sub>O<sub>3</sub> and  $\alpha$ -Al<sub>2</sub>O<sub>3</sub>. This noticeably reduces the critical concentration of Cr or/and Al of the alloy for Cr<sub>2</sub>O<sub>3</sub> or  $\alpha$ -Al<sub>2</sub>O<sub>3</sub> scale formation, plausibly converting a non-oxidation-resistant alloy to an oxidation-resistant one. The metal NPs which are able to be oxidized into hcp oxides play a similar seeding effect. So far, there have been little studies on the theory and practice of applying NPs to catalyze desired selective oxidation of alloys. The mechanism involved and the relationships between crucial parameters (e.g. size, dispersion density and uniformity) and properties (e.g. thermodynamic stability, thermostability)

of the specific NPs with the Cr or/and Al concentration of alloys deserve to be deeply and extensively explored in the future.

Oxidation of  $M_xAl_y$  like  $Ni_2Al_3$  preferentially grows  $\theta$ - or/and  $\gamma$ -  $Al_2O_3$  rather than  $\alpha$ - $Al_2O_3$ , because  $\alpha$ - $Al_2O_3$  formation through the metal-stable-to-stable alumina transformation route needs to overcome smaller nucleation energy barrier. However, The slow alumina phase transformation kinetics causes faster oxidation. It is meaningful to explore a method to facilitate the transformation process. Dispersion of NPs of hcp metal oxides (e.g.,  $Cr_2O_3$ ,  $\alpha$ - $Al_2O_3$ ) into  $M_xAl_y$  appears to be an effective method to be applied to promote the alumina phase transformation. In particular,  $\alpha$ - $Al_2O_3$  can directly grow if those hcp oxide NPs are dispersed onto the intermetallic alloy surface. Rutile  $TiO_2$  NPs are also able to catalyze  $\alpha$ - $Al_2O_3$  thermal growth. This highlights the significance of the hcp oxygen sublattice structure in exerting the template effect on the corundum TGO formation. There is no nucleation energy barrier for the thermal growth of  $\alpha$ - $Al_2O_3$  on typical crystal planes of the NPs of the oxides with hexagonal oxygen sublattice structure.

$RE_xO_y$  addition behaves similarly to RE alloying in slowing down the oxidation of alloys. The REE effect seems to work after  $RE_xO_y$  dispersions in alloys have been swept over by inward growing TGO, because  $RE_xO_y$  in it easier decompose to produce RE ions. This is a crucial step before RE ions segregate to the GBs in TGO or blocking the short-circuit diffusion of species (primarily cations) for oxide growth. Based on the dependence of thermodynamic stability of particles on dimension,  $RE_xO_y$  NP is more effective than MP to take the REE on TGO kinetic growth through the RE oxide GB segregation model. When  $RE_xO_y$  NP is sized to a critical value below which the NP itself is not stable at high temperatures,  $RE_xO_y$  decomposes to produce elementary RE in alloys. On this basis, an extreme low solubility limit of RE in alloys would cause it to form second-phase particles containing RE and O (because RE has a strong affinity for O) and, the finer NPs among them may positively affect oxidation kinetics.

Some metal NPs and metal oxide NPs can be applied as key constituents to develop chromia- and alumina-forming coatings. They are hopeful to be used as templates and seeds for thermally growing  $Cr_2O_3$  and  $\alpha$ - $Al_2O_3$ . Nano-sized  $RE_xO_y$  dispersions with respect to micron-sized counterparts play a greater role in slowing down TGO growth. Further widespread studies should be carried out in nanoscale and even atomic scale for providing deep insights into the mechanism of nanosize effect on oxidation of the concerned particles. This will help us better understand how  $Cr_2O_3$  and  $\alpha$ - $Al_2O_3$  nucleate and steadily grow on alloys from the perspective of microstructure. And last but not least, NPs tend to agglomerate. Agglomeration of the NPs applied to alloys and coatings undoubtedly have unbeneficial impact on oxidation. Uniform dispersion is a matter of importance to the concerned NPs which can exert the nanosize effects to the maximum extent.

**Acknowledgements** The work is supported by Key project of Jiangxi Provincial Natural Science Foundation (project Grant No. 20181ACB20009) and National Natural Science Foundation of China (NSFC, project Grant No. 51771088).

**Author Contributions** XP Conceptualization, Supervision, Writing-Review and editing, Funding acquisition, Project administration. YH Investigation, Formal analysis. Xiaolan Wang: Investigation, Formal analysis. YX Data curation, Writing - Original draft.

## Declarations

**Conflict of Interest** The authors declare that they have no conflict of interest.

## References

1. H. Gleiter, *Progress Mater. Sci.* **33**, 1989 (223).
2. H. Gleiter, *Acta Materialia*. **48**, 2000 (1).
3. C. Suryanarayana, *International Materials Reviews*. **40**, 1995 (41).
4. S. C. Tjong and H. Chen, *Materials Science and Engineering: R: Reports*. **45**, 2004 (1).
5. B. V. Mahesh and R. K. Singh Raman, *Metallurgical and Materials Transactions A*. **45**, 2014 (5799).
6. X. Peng and F. Wang, Chapter 15: Oxidation Resistant Nanocrystalline Coatings. in *Developments in High Temperature Corrosion and Protection of Materials*, Woodhead Pub Ltd. eds. W. Gao and Z. Li (Cambridge, England, UK, 2008).
7. C. Wagner, *Z. Elektrochem* **63**, (7), 1959 (772).
8. Z. Huang, X. Peng, C. Xu, and F. Wang, *Journal of The Electrochemical Society*. **156**, 2009 (C95).
9. G. Liu, J. Lu, and K. Lu, *Materials Science and Engineering: A*. **286**, 2000 (91).
10. Y. Huang, X. Peng, Z. Dong, and Y. Cui, *Corrosion Science*. **143**, 2018 (76).
11. S. S. Rajahram, T. J. Harvey, J. C. Walker, S. C. Wang, R. J. K. Wood, and G. Lalev, *Wear*. **271**, 2011 (1302).
12. A. A. Tchizhik, A. I. Rybnikov, I. S. Malashenko, S. A. Leontiev, and A. S. Osyka, *Surface and Coatings Technology*. **78**, 1996 (113).
13. Z. Liu, W. Gao, K. L. Dahm, and F. Wang, *Acta Materialia*. **46**, 1998 (1691).
14. M. H. Li, Z. Y. Zhang, X. F. Sun, J. G. Li, F. S. Yin, W. Y. Hu, and Z. Q. Hu, *Surface and Coatings Technology*. **165**, 2003 (241).
15. X. Peng, J. Yan, Y. Zhou, and F. Wang, *Acta Materialia*. **53**, 2005 (5079).
16. X. Peng and F. Wang, *Corrosion Science*. **45**, 2003 (2293).
17. S. Veprek, M. Haussmann, S. Reiprich, L. Shizhi, and J. Dian, *Surface and Coatings Technology*. **86**, 1996 (394).
18. M. Amaral, F. Mohasseb, F. J. Oliveira, F. Benedic, R. F. Silva, and A. Gicquel, *Thin Solid Films*. **482**, 2005 (232).
19. M. L. Lau, E. Strock, A. Fabel, C. J. Lavernia, and E. J. Lavernia, *Nanostructured Materials*. **10**, 1998 (723).
20. D. Stover, G. Pracht, H. Lehmann, M. Dietrich, J. E. Doring, and R. Vassen, *Journal of Thermal Spray Technology*. **13**, 2004 (76).
21. P. Richer, M. Yandouzi, L. Beauvais, and B. Jodoin, *Surface and Coatings Technology*. **204**, 2010 (3962).
22. J. A. Picas, A. Forn, A. Igartua, and G. Mendoza, *Surface and Coatings Technology*. **174**, 2003 (1095).
23. X. Yang, X. Peng, C. Xu, and F. Wang, *Journal of the Electrochemical Society*. **156**, 2009 (C167).
24. X. Peng, *Nanoscale*. **2**, 2010 (262).
25. H. Zhen and X. Peng, *Surface and Coatings Technology*. **352**, 2018 (541).
26. X. Peng, H. Zhen, L. Tian, X. Wang, K. Wang, and Y. Xie, *Composites Part B: Engineering*. **234**, 2022 (109721).
27. W. Lewandowski, et al., *Nat. Commun.* **4**, 2015 (9590).
28. S. F. Chen, J. P. Li, K. Qian, W. P. Xu, Y. Lu, W. X. Huang, and S. H. Yu, *Nano Research*. **3**, 2010 (244).
29. J. Rozra, I. Saini, A. Sharma, N. Chandak, S. Aggarwal, R. Dhiman, and P. K. Sharma, *Materials Chemistry and Physics*. **134**, 2012 (1121).
30. J. Ouyang, C. W. Chu, C. R. Szmamda, L. Ma, and Y. Yang, *Nature Materials*. **3**, 2004 (918).



31. R. R. Kakarla, K. P. Lee, and A. I. Gopalan, *Journal of nanoscience and nanotechnology*. **7**, 2007 (3117).
32. S. Mahendia, P. K. Goyal, A. K. Tomar, R. P. Chahal, and S. Kumar, *Journal of Electronic Materials*. **45**, 2016 (5418).
33. S. P. Solodovnikov, L. M. Bronshtein, O. A. Platonova, T. P. Loginova, E. A. Yudanov, M. A. Apresova, I. A. Khotina, and P. M. Valetskii, *Polymer Science Series A*. **55**, 2013 (749).
34. J. S. Garitaonandia, M. Insausti, E. Goikolea, M. Suzuki, J. D. Cashion, N. Kawamura, H. Ohsawa, I. G. De Muro, K. Suzuki, F. Plazaola, and T. Rojo, *Nano Letters*. **8**, 2008 (661).
35. Y. Ju, X. Li, J. Feng, Y. Ma, J. Hu, and X. Chen, *Applied surface science*. **316**, 2014 (132).
36. M. Muhlberg, *Journal of Materials Chemistry A*. **5**, 2017 (9465).
37. Y. Z. Li, Z. J. Wang, Y. Bai, W. Liu, and Z. D. Zhang, *Journal of the American Ceramic Society*. **102**, 2019 (5253).
38. G. Centi and S. Perathoner, *European Journal of Inorganic Chemistry*. **26**, 2009 (3851).
39. J. W. Xu, K. Yao, and Z. K. Xu, *Nanoscale*. **11**, 2019 (8680).
40. K. Schaefer and A. Miszczyk, *Corrosion Science*. **66**, 2013 (380).
41. S. Y. Arman, B. Ramezanzadeh, S. Farghadani, M. Mehdipour, and A. Rajabi, *Corrosion Science*. **77**, 2013 (118).
42. X. Zhang, F. Wang, and Y. Du, *Surface and Coatings Technology* **201**, 2007 (7241).
43. Y. Shao, Y. Li, Y. Du, and F. Wang, *Corrosion*. **62**, 2006 (483).
44. L. L. Xue, L. K. Xu, and Q. F. Li, *Journal of Materials Sciences and Technology*. **23**, 2007 (563).
45. A. Madhankumar, S. Nagarajan, N. Rajendran, and T. Nishimura, *Journal of Solid State Electrochemistry*. **16**, 2012 (2085).
46. R. W. Armstrong, B. Baschung, D. W. Booth, and M. Samirant, *Nano Letters*. **3**, 2003 (253).
47. S. T. Khan, A. A. Al-Khedhairi, and J. Musarrat, *Journal of Nanoparticle Research*. **17**, 2015 (276).
48. X. Q. Liu, J. Iocozzia, Y. Wang, X. Cui, Y. H. Chen, S. Q. Zhao, Z. Li, and Z. Q. Lin, *Energy & Environmental Science*. **10**, 2017 (402).
49. Z. Pei, X. Zheng, and Z. Li, *Journal of Nanoscience and Nanotechnology*. **16**, 2016 (4655).
50. N. Yadav, *3 Biotech*. **12**, 2022 (121).
51. P. Kofstad, *High temperature corrosion*, (Elsevier Applied Science Publisher, New York, 1988).
52. D. J. Young, *High Temperature Oxidation and Corrosion of Metals*, (Elsevier, Sydney, 2016), pp. 193–260.
53. J. Zhao, X. Peng, Y. Wang, and F. Wang, *Acta Materialia*. **55**, 2007 (3193).
54. N. Gugliemi, *Journal of the Electrochemical Society*. **119**, 1972 (1009).
55. G. Palumbo, D. M. Doyle, A. M. El-Sherik, U. Erb, and K. T. Aust, *Scripta Metallurgica et Materialia*. **25**, 1991 (679).
56. Y. Zhang, X. Peng, and F. Wang, *Materials Letters*. **58**, 2004 (1134).
57. Z. Dong, Y. Xie, and X. Peng, *Corrosion Science*. **194**, 2022 (109915).
58. Z. Dong, X. Peng, Y. Guan, L. Li, and F. Wang, *Corrosion Science*. **62**, 2012 (147).
59. X. Peng, L. Li, and F. Wang, *Scripta Materialia*. **60**, 2009 (699).
60. C. Zhang, X. Peng, J. Zhao, and F. Wang, *Journal of the Electrochemical Society*. **152**, 2005 (B321).
61. P. Villars, A. Prince, and H. Okamoto, *Handbook of Ternary Alloy Phase Diagrams*, (ASM International, Mater Park, USA, 1997).
62. D. A. Porter and K. E. Easterling, *Phase Transformation in Metals and Alloys*, (Chapman & Hall, London, 1992), p. 60.
63. Y. Niu, Z. Q. Cao, F. Gesmundo, G. Farnè, G. Randi, and C. L. Wang, *Corrosion Science*. **45**, 2003 (1125).
64. Z. Huang, X. Peng, and F. Wang, *Oxidation of Metals*. **65**, 2006 (223).
65. Z. Huang, X. Peng, C. Xu, and F. Wang, *Journal of Materials Research*. **22**, 2007 (3166).
66. Y. Zhou, X. Peng, and F. Wang, *Oxidation of Metals*. **64**, 2005 (169).
67. D. F. Susan, A. R. Marder, and K. Barmak, *Thin Solid Films*. **307**, 1997 (133).
68. D. F. Susan and A. R. Marder, *Oxidation of metals*. **57**, 2002 (159).
69. X. Peng, M. Li, and F. Wang, *Corrosion Science*. **53**, 2011 (1616).
70. X. Yang, X. Peng, and F. Wang, *Scripta Materialia*. **56**, 2007 (509).
71. X. Yang, X. Peng, and F. Wang, *Scripta Materialia*. **56**, 2007 (891).
72. H. Zhen and X. Peng, *Corrosion Science*. **150**, 2019 (121).

73. D. P. Whittle and J. Stringer, *Philosophical Transactions of the Royal Society of London Series A, Mathematical and Physical Sciences*. **295**, 1980 (309).
74. D. P. Moon, *Materials Science and Technology*. **5**, 1989 (754).
75. J. Jedlinski, *Solid State Phenomena*. **21&22**, 1992 (335).
76. W. J. Quadackers and L. Singheiser, *Materials Science Forum*. **369–372**, 2001 (77).
77. B.A. Pint, Progress in understanding the reactive element effect since the Whittle and Stringer literature review in Proc. John Stringer Symp. on High Temp. Corrosion. (eds Tortorelli, P.F. and Hou, P.Y.) 27 – 37 (Ohio, 2003).
78. P. Y. Hou, *Materials Science Forum*. **696**, 2011 (39).
79. J. Forster, B. P. Cameron, and J. A. Carews, *Transactions of the IMF*. **63**, 1985 (115).
80. J. Foster, et al. U.K. Patent GB2167446 (1986), also *U.S. Patent*. 4,789,441, 1988.
81. F. J. Honey, E. C. Kedward, and V. Wride, *Journal of Vacuum Science & Technology A: Vacuum, Surfaces, and Films*. **4**, 1986 (2593).
82. Y. Zhang, *Jom*. **67**, 2015 (2599).
83. B. L. Bates, L. Z. Zhang, and Y. Zhang, *Surface Engineering*. **31**, (3), 2015 (202).
84. Y. Xie, L. Tian, L. You, X. Peng, Development and high-temperature corrosion performance of MCrAl(Y) coatings prepared by electrochemical deposition: A brief review, this issue of the journal.
85. C. Wagner, *Journal of the electrochemical Society*. **99**, 1952 (369).
86. D. L. Douglass, *Corrosion Science*. **8**, 1968 (665).
87. Y. Xie, Y. Huang, Y. Li, and X. Peng, *Corrosion Science*. **190**, 2021 (109717).
88. I. Levin and D. Brandon, *Journal of the American Ceramic Society*. **81**, 1998 (1995).
89. P. Euzen, P. Raybaud, X. Krokidis, H. Toulhoat, J. L. Le Loarer, J. P. Jolivet, and C. Froidefond, *Alumina*, (Handbook of porous solids, 2002), p. 1591.
90. S. L. Shang, Y. Wang, and Z. K. Liu, *Applied Physics Letters*. **90**, 2007 (349).
91. M. W. Brumm and H. J. Grabke, *Corrosion Science*. **33**, 1992 (1677).
92. J. Doychak, J. L. Smialek, and T. E. Mitchell, *Metallurgical Transactions A*. **20**, 1989 (499).
93. E. Schumann, *Oxidation of Metals*. **43**, 1995 (157).
94. V. Tolpygo and D. R. Clarke, *Materials at High Temperatures*. **17**, 2000 (59).
95. X. Peng, T. Li, and W. P. Pan, *Scripta Materialia*. **44**, 2001 (1033).
96. E. D. Specht, P. F. Tortorelli, and P. Zschack, *Powder Diffraction*. **19**, 2004 (69).
97. P. Y. Hou, A. P. Paulikas, and B. W. Veal, *Materials Science Forum*. **461–464**, 2004 (671).
98. L. Zheng, X. Peng, and F. Wang, *Corrosion Science*. **53**, 2011 (597).
99. W. Ren, Q. Li, J. Song, C. Xiao, Z. Xu, L. He, and C. Cao, *Materials Research Innovations*. **18**, 2015 (945).
100. B. A. Pint, J. R. Martin, and L. W. Hobbs, *Solid State Ionics*. **78**, 1995 (99).
101. X. F. Zhang, K. Thaidigsmann, J. Ager, and P. Y. Hou, *Journal of Materials Research*. **21**, 2006 (1409).
102. P. Brito, H. Pinto, C. Genzel, M. Klaus, and A. Kaysser-Pyzalla, *Acta Materialia*. **60**, 2012 (1230).
103. P. Brito, H. Pinto, and A. Kostka, *Corrosion Science*. **105**, 2016 (100).
104. B. A. Pint, M. Treska, and L. W. Hobbs, *Oxidation of Metals*. **47**, 1997 (1).
105. P. Burtin, J. P. Brunelle, M. Pijolat, and M. Soustelle, *Applied Catalysis*. **34**, 1987 (225).
106. Y. Kitajima, S. Hayashi, T. Nishimoto, T. Narita, and S. Ukai, *Oxidation of Metals*. **73**, 2010 (375).
107. Y. Huang and X. Peng, *Corrosion Science*. **112**, 2016 (226).
108. C. Xu, X. Peng, and F. Wang, *Corrosion Science*. **52**, 2010 (740).
109. X. Tan, X. Peng, and F. Wang, *Corrosion Science*. **85**, 2014 (280).
110. D. M. Lipkin and D. R. Clarke, *Oxidation of Metals*. **45**, 1996 (267).
111. X. Peng, D. R. Clarke, and F. Wang, *Oxidation of Metals*. **60**, 2003 (225).
112. J. M. McHale, A. Auroux, A. J. Perrotta, and A. Navrotsky, *Science*. **277**, 1997 (788).
113. Y. Huang, X. Peng, and X.-Q. Chen, *Corrosion Science*. **153**, 2019 (109).
114. S. Kachi, K. Momiyama, and S. Shimizu, *Journal of the Physical Society of Japan*. **18**, 1963 (106).
115. Y. Huang, X. Peng, and X.-Q. Chen, *Journal of Alloys and Compounds*. **863**, 2021 (158666).
116. A. Khan, Y. Huang, Z. Dong, and X. Peng, *Corrosion Science*. **150**, 2019 (91).
117. A. Khan, Z. Dong, and X. Peng, *Surface and Coatings Technology*. **384**, 2020 (125861).
118. X. Wang, X. Peng, Development of nickel aluminide coating with increased oxidation resistance: Externally or internally dispersing TiO<sub>2</sub> nanoparticles, in preparation.
119. L.B. Pfeil, Improvement in Heat-resisting Alloys. *UK Patent*, No. 459848 (1937).

120. W. D. Klopp, *Aerospace Structural Metals Handbook, Code4106*, (Purdue Research Foundation, West Lafayette, 1992), p. 1.
121. T. A. Ramanarayanan, R. Ayer, R. Petkovic-Luton, and D. P. Leta, *Oxidation of Metals*. **29**, 1988 (445).
122. M. C. García-Alonso, J. L. González-Carrasco, M. L. Escudero, and J. Chao, *Oxidation of Metals*. **53**, 2000 (77).
123. S. Weinbruch, A. Anastasiadis, H. M. Ortner, H. P. Martinz, and P. Wilhartitz, *Oxidation of metals*. **51**, 1999 (111).
124. Y. Z. Shen, T. T. Zou, S. Zhang, and L. Z. Sheng, *ISIJ international*. **53**, 2013 (304).
125. A. O. F. Hayama, H. R. Z. Sandim, J. F. C. Lins, M. F. Hupaló, and A. F. Padilha, *Materials Science and Engineering: A*. **371**, 2004 (198).
126. T. A. Ramanarayanan, M. Raghavan, and R. Petkovic-Luton, *Journal of the Electrochemical Society*. **131**, 1984 (923).
127. K. L. Luthra and C. L. Briant, *Oxidation of metals*. **26**, 1986 (397).
128. C. M. Cotell, G. J. Yurek, R. J. Hussey, D. F. Mitchell, and M. J. Graham, *Journal of the Electrochemical Society*. **134**, 1987 (1871).
129. K. Przybylski, A. J. Garratt-Reed, B. A. Pint, E. P. Katz, and G. J. Yurek, *Journal of the Electrochemical Society*. **134**, 1987 (3207).
130. B. A. Pint, A. J. Garratt-Reed, and L. W. Hobbs, *Materials at High Temperatures*. **13**, 1995 (3).
131. X. Peng, D. Ping, T. Li, and W. Wu, *Journal of the Electrochemical Society*. **145**, 1998 (389).
132. X. Peng, *Oxidation of metals*. **51**, 1999 (291).
133. P. W. Tasker and D. M. Duffy, *Philosophical Magazine A*. **47**, 1983 (L45).
134. D. M. Duffy and P. W. Tasker, *Philosophical Magazine A*. **54**, 1986 (759).
135. F. N. Rhines and R. G. Gonnell Jr., *Journal of the Electrochemical Society*. **124**, 1977 (1122).
136. A. Atkinson, R. I. Taylor, and P. D. Goode, *Oxidation of metals*. **13**, 1979 (519).
137. A. Atkinson, R. I. Taylor, and A. F. Hughes, *Philosophical Magazine A*. **45**, 1982 (823).
138. A. Atkinson and D. J. Smart, *Journal of the Electrochemical Society*. **135**, 1988 (2886).
139. X. Peng, J. Yan, L. Zheng, and C. Xu, *Materials and Corrosion*. **62**, 2011 (514).
140. J. Yan, X. Peng, and F. Wang, *Materials Science and Engineering: A*. **426**, 2006 (26).
141. X. Peng, J. Yan, Z. Dong, C. Xu, and F. Wang, *Corrosion Science*. **52**, 2010 (1863).
142. H. Zhang, X. Peng, J. Zhao, and F. Wang, *Electrochemical and solid-state letters*. **19**, 2007 (C13).
143. X. Peng, Y. Guan, Z. Dong, C. Xu, and F. Wang, *Corrosion Science*. **53**, 2011 (1984).
144. X. Wang, X. Peng, X. Tan, and F. Wang, *Scientific Reports*. **6**, 2016 (29593).
145. B. A. Pint, *Oxidation of Metals*. **45**, 1996 (1).

**Publisher's Note** Springer Nature remains neutral with regard to jurisdictional claims in published maps and institutional affiliations.

Springer Nature or its licensor (e.g. a society or other partner) holds exclusive rights to this article under a publishing agreement with the author(s) or other rightsholder(s); author self-archiving of the accepted manuscript version of this article is solely governed by the terms of such publishing agreement and applicable law.